

# New relativistic effective interaction for finite nuclei, infinite nuclear matter and neutron stars

Bharat Kumar<sup>1,2</sup>, S. K. Patra<sup>1,2</sup>, and B. K. Agrawal<sup>2,3</sup>

<sup>1</sup>*Institute of Physics, Bhubaneswar-751005, India*

<sup>2</sup>*Homi Bhabha National Institute, Training School Complex, Anushakti Nagar, Mumbai 400085, India and*

<sup>3</sup>*Saha Institute of Nuclear Physics, 1/AF, Bidhannagar, Kolkata - 700064, India.*

(Dated: February 8, 2018)

We carry out the study for finite nuclei, infinite nuclear matter and neutron star properties with the newly developed relativistic force named as the Institute Of Physics Bhubaneswar-I(IOPB-I). Using this force, we calculate the binding energies, charge radii and neutron-skin thickness for some selected nuclei. From the ground state properties of superheavy nuclei ( $Z=120$ ), it is noticed that considerable shell gaps appear at neutron numbers  $N=172$ ,  $184$  and  $198$ , manifesting the magicity at these numbers. The low-density behavior of the equation of state for pure neutron matter is compatible with other microscopic models. Along with the nuclear symmetry energy, its slope and curvature parameters at the saturation density are consistent with those extracted from various experimental data. We calculate the neutron star properties with the equation of state composed of nucleons and leptons in *beta - equilibrium* which are in good agreement with the X-ray observations by Steiner and Nättilä. Based on the recent observation GW170817 with a quasi-universal relation, L. Rezzolla *et al.* have set a limit for the maximum mass that can be supported against gravity by a nonrotating neutron star is in the range  $2.01 \pm 0.04 \lesssim M(M_{\odot}) \lesssim 2.16 \pm 0.03$ . We find that the maximum mass of the neutron star for the IOPB-I parametrization is  $2.15M_{\odot}$ . The radius and tidal deformability of a *canonical* neutron star mass  $1.4M_{\odot}$  are  $13.2$  km and  $3.9 \times 10^{36}$  g cm<sup>2</sup> s<sup>2</sup> respectively.

PACS numbers: 26.60.+c, 26.60.Kp, 95.85.Sz

## I. INTRODUCTION

In the present scenario nuclear physics and nuclear astrophysics are well described within the self-consistent effective mean field models [1]. These effective theories are not only successful to describe the properties of finite nuclei but also explain the nuclear matter at supra normal densities [2]. Recently, a large number of nuclear phenomena have been predicted near the nuclear drip-lines within the relativistic and non-relativistic formalisms [3–5]. Consequently, several experiments are planned in various laboratories to probe deeper side of the unknown nuclear territories, *i.e.*, the neutron and proton drip-lines. Among the effective theories, the relativistic mean field (RMF) model is one of the most successful self-consistent formalism, which has currently drawn attention for theoretical studies of such systems.

Although, the construction of the energy density functional for the RMF model is different than those for the non-relativistic models, such as Skyrme [6, 7] and Gogny interactions [8], the obtained results for finite nuclei are in general very close to each other. The same accuracy in prediction is also valid for the properties of the neutron stars. At higher densities, the relativistic effects are accounted appropriately within the RMF model [9]. In the RMF model the interactions among nucleons are described through the exchange of mesons. These mesons are collectively taken as effective fields and denoted by classical numbers, which are the quantum mechanical expectation values. In brief, the RMF formalism is the relativistic Hartree or Hartree Fock approximations to the one boson exchange (OBE) theory of nuclear interactions. In OBE theory, the nucleons interact with each other by exchange of isovector  $\pi$ -,  $\rho$ -, and  $\delta$ -mesons and isoscalars like  $\eta$ -,  $\rho$ -, and  $\omega$ - mesons. The  $\pi$ -, and  $\eta$ -mesons are pseudo-scalar in nature and do not obey the ground state par-

ity symmetry. In mean-field level, they do not contribute to the ground state properties of even nuclei.

The first and simple successful relativistic Lagrangian is formed by taking only the  $\sigma$ -,  $\omega$ - and  $\rho$ - mesons contribution into account without any non-linear term to the Lagrangian density. This model predicts an unreasonably large incompressibility  $K$  of  $\sim 550$  MeV for the infinite nuclear matter at saturation [9]. In order to lower the value of  $K$  to an acceptable range, the self-coupling terms in sigma meson are included by Boguta and Bodmer [10]. Based on this Lagrangian density, a large number of parameter sets, such as NL1 [11], NL2 [11], NL-SH [12], NL3 [13] and NL3\* [14] were calibrated. The addition of  $\sigma$ -meson self-couplings improved the quality of finite nuclei properties and incompressibility remarkably. However, the equation of states at supra-normal densities were quite stiff. Thus, the addition of vector meson self-coupling is introduced into the Lagrangian density and different parameter sets are constructed [15–17]. These parameter sets are able to explain the finite nuclei and nuclear matter properties to a great extent, but the existence of the Coester-band as well as the 3-body effects need to be addressed. Subsequently, nuclear physicists also change their way of thinking and introduced different strategies to improve the result by designing the density-dependent coupling constants and effective field theory motivated relativistic mean field (E-RMF) model [1, 18].

Further, motivated by the effective field theory, Furnstahl *et al.* [1] used all possible couplings up to fourth order of the expansion, exploiting the naive dimensional analysis (NDA) and naturalness, obtained the G1 and G2 parameter sets. In the Lagrangian density, they considered only the contributions of the isoscalar-isovector cross-coupling, which has a greater implication on neutron radius and equation of state (EoS) of asymmetric nuclear matter [19]. Later on it is realized that the contributions of  $\delta$ -mesons are also needed to explain cer-

tain properties of nuclear phenomena in extreme conditions [20, 21]. Though the contributions of the  $\delta$ -mesons to the bulk properties are nominal in the normal nuclear matter, but effects are significant for highly asymmetric dense nuclear matter. The  $\delta$  meson splits the effective masses of proton and neutron, which influences the production of  $K^{+,-}$  and  $\pi^{+}/\pi^{-}$  in the heavy ion collision (HIC) [22]. Also, it increases the proton fraction in the  $\beta$ -stable matter and modifies the transport properties of neutron star and heavy ion reactions [23–25]. The source terms for both the  $\rho$ - and  $\delta$ -mesons contain isospin density, but their origins are different. The  $\rho$ -meson arises from the asymmetry in the number density and the evolution of the  $\delta$ -meson is from the mass asymmetry of the nucleons. The inclusion of  $\delta$ -mesons could influence the certain physical observables like neutron-skin thickness, isotopic shift, two neutron separation energy  $S_{2n}$ , symmetry energy  $S(\rho)$ , giant dipole resonance (GDR) and effective mass of the nucleons, which are correlated with the isovector channel of the interaction. The density dependence of symmetry energy is strongly correlated with the neutron-skin thickness in heavy nuclei, but till now experiments have not fixed the accurate value of neutron radius, which is under consideration for verification in the parity-violating electron-nucleus scattering experiments [18, 26].

Recently, the detection of gravitational waves from binary neutron star GW170817 is a major breakthrough in astrophysics which is detected for the first time by the advanced Laser Interferometer Gravitational-wave Observatory (aLIGO) and advanced VIRGO detectors [27]. This detection has certainly posed to be a valuable guidance to study the matter under the most extreme conditions. Inspiring and coalescing objects of a binary neutron star result in gravitational waves. Due to the merger, a compact remnant is remaining whose nature is decided by two factors *i.e* (i) the masses of the inspiraling objects and (ii) the equation of state of the neutron star matter. For final state, the formation of either a neutron star or a black hole depends on the masses and stability of the objects. The chirp mass is measured very precisely from data analysis of GW170817 and it is found to be  $1.188_{-0.002}^{+0.004} M_{\odot}$  for the 90% credible intervals. It is suggested that total mass should be  $2.74_{-0.01}^{+0.04} M_{\odot}$  for low-spin priors and  $2.82_{-0.09}^{+0.47} M_{\odot}$  for high-spin priors [27]. Moreover, the maximum mass of nonspinning neutron stars (NSs) as a function of radius are observed with the highly precise measurements of  $M \approx 2.0 M_{\odot}$ . From the observations of gravitational waves, we can extract information regarding the radii or tidal deformability of the nonspinning and spinning NSs [28–30]. Once we succeed in getting this information, it is easy to get the neutron star matter equation of state [31, 32].

In present paper, we constructed a new parameter set IOPB-

I using the simulated annealing method (SAM) [33–35] and explore the generic prediction of properties of finite nuclei, nuclear matter and neutron stars within the E-RMF formalism. Our new parameter set yields the considerable shell gap appearing at neutron numbers  $N=172, 184$  and  $198$  showing the magicity of these numbers. The behavior of the density-dependent symmetry energy of nuclear matter at low and high densities are examined in detail. The effect of the core EoS on the mass, radius and tidal deformability of an NS are evaluated using the static  $l = 2$  perturbation of a Tolman-Oppenheimer-Volkoff solution.

The paper is organized as follows: In Sec. II, we outline the effective field theory motivated relativistic mean field (E-RMF) Lagrangian. We outline briefly the equations of motion for finite nuclei and equation of states (EoS) for infinite nuclear matter. In Sec. III, we discuss the strategy of the parameter fitting using the simulated annealing method (SAM). After getting the new parameter set IOPB-I, the results on binding energy, two neutron separation energy, neutron-skin thickness for finite nuclei are discussed in Sec. IVA. In sub-Sec. IVB and IVC, the EoS for symmetric and asymmetric matters are presented. The mass-radius and tidal deformability of the neutron star obtained by the new parameter set is also discussed in this section. Finally, the summary and concluding remarks are given in Sec. V.

*Conventions:* We have taken the value of  $G = c = 1$  throughout the manuscript.

## II. FORMALISM

### A. Energy density functional and equations of motion

In this section, we outline briefly the E-RMF Lagrangian [1]. The beauty of effective Lagrangian is that, one can ignore the basic difficulties of the formalism, like renormalization and divergence of the system. The model can be used directly by fitting the coupling constants and some masses of the mesons. The E-RMF Lagrangian has an infinite number of terms with all types of self and cross couplings. It is necessary to develop a truncation procedure for practical use. Generally, the meson fields constructed in the Lagrangian are smaller than the mass of the nucleon. Their ratio could be used as a truncation scheme as it is done in Refs. [1, 3, 36, 37] along with the NDA and naturalness properties. The basic nucleon-meson E-RMF Lagrangian (with  $\delta$ -meson,  $W \times R$ ) up to 4<sup>th</sup> order with exchange mesons like  $\sigma$ -,  $\omega$ -,  $\rho$ -meson and photon  $A$  is given as [1, 38]:

$$\begin{aligned}
\mathcal{E}(r) = & \sum_{\alpha} \varphi_{\alpha}^{\dagger}(r) \left\{ -i\boldsymbol{\alpha} \cdot \boldsymbol{\nabla} + \beta [M - \Phi(r) - \tau_3 D(r)] + W(r) + \frac{1}{2} \tau_3 R(r) + \frac{1 + \tau_3}{2} A(r) \right. \\
& - \frac{i\beta\boldsymbol{\alpha}}{2M} \cdot \left( f_{\omega} \boldsymbol{\nabla} W(r) + \frac{1}{2} f_{\rho} \tau_3 \boldsymbol{\nabla} R(r) \right) \left. \right\} \varphi_{\alpha}(r) + \left( \frac{1}{2} + \frac{\kappa_3}{3!} \frac{\Phi(r)}{M} + \frac{\kappa_4}{4!} \frac{\Phi^2(r)}{M^2} \right) \frac{m_s^2}{g_s^2} \Phi^2(r) \\
& - \frac{\zeta_0}{4!} \frac{1}{g_{\omega}^2} W^4(r) + \frac{1}{2g_s^2} \left( 1 + \alpha_1 \frac{\Phi(r)}{M} \right) (\boldsymbol{\nabla} \Phi(r))^2 - \frac{1}{2g_{\omega}^2} \left( 1 + \alpha_2 \frac{\Phi(r)}{M} \right) \\
& (\boldsymbol{\nabla} W(r))^2 - \frac{1}{2} \left( 1 + \eta_1 \frac{\Phi(r)}{M} + \frac{\eta_2}{2} \frac{\Phi^2(r)}{M^2} \right) \frac{m_{\omega}^2}{g_{\omega}^2} W^2(r) - \frac{1}{2e^2} (\boldsymbol{\nabla} A(r))^2 - \frac{1}{2g_{\rho}^2} (\boldsymbol{\nabla} R(r))^2 \\
& - \frac{1}{2} \left( 1 + \eta_{\rho} \frac{\Phi(r)}{M} \right) \frac{m_{\rho}^2}{g_{\rho}^2} R^2(r) - \Lambda_{\omega} (R^2(r) \times W^2(r)) + \frac{1}{2g_{\delta}^2} (\boldsymbol{\nabla} D(r))^2 + \frac{1}{2} \frac{m_{\delta}^2}{g_{\delta}^2} (D^2(r)) , \quad (1)
\end{aligned}$$

where  $\Phi$ ,  $W$ ,  $R$ ,  $D$  and  $A$  are the fields,  $g_{\sigma}$ ,  $g_{\omega}$ ,  $g_{\rho}$ ,  $g_{\delta}$ ,  $\frac{e^2}{4\pi}$  are the coupling constants and  $m_{\sigma}$ ,  $m_{\omega}$ ,  $m_{\rho}$  and  $m_{\delta}$  are the masses for  $\sigma$ ,  $\omega$ ,  $\rho$ ,  $\delta$  mesons and photon, respectively.

Now, our aim is to solve the field equations for the baryons and mesons (nucleon,  $\sigma$ ,  $\omega$ ,  $\rho$ ,  $\delta$ ) using the variational principle. We obtained the mesons equation of motion using the equation  $\left( \frac{\partial \mathcal{E}}{\partial \phi_i} \right)_{\rho=constant} = 0$ . The single particle energy for the nucleons is obtained by using the Lagrange multiplier  $\varepsilon_{\alpha}$ , which is the energy eigenvalue of the Dirac equation con-

straining the normalization condition  $\sum_{\alpha} \varphi_{\alpha}^{\dagger}(r) \varphi_{\alpha}(r) = 1$  [39]. The Dirac equation for the wave function  $\varphi_{\alpha}(r)$  becomes

$$\frac{\partial}{\partial \varphi_{\alpha}^{\dagger}(r)} \left[ \mathcal{E}(r) - \sum_{\alpha} \varphi_{\alpha}^{\dagger}(r) \varphi_{\alpha}(r) \right] = 0, \quad (2)$$

*i.e.*

$$\begin{aligned}
& \left\{ -i\boldsymbol{\alpha} \cdot \boldsymbol{\nabla} + \beta [M - \Phi(r) - \tau_3 D(r)] + W(r) + \frac{1}{2} \tau_3 R(r) + \frac{1 + \tau_3}{2} A(r) \right. \\
& \left. - \frac{i\beta\boldsymbol{\alpha}}{2M} \cdot \left[ f_{\omega} \boldsymbol{\nabla} W(r) + \frac{1}{2} f_{\rho} \tau_3 \boldsymbol{\nabla} R(r) \right] \right\} \varphi_{\alpha}(r) = \varepsilon_{\alpha} \varphi_{\alpha}(r). \quad (3)
\end{aligned}$$

The mean-field equations for  $\Phi$ ,  $W$ ,  $R$ ,  $D$  and  $A$  are given by

$$\begin{aligned}
-\Delta\Phi(r) + m_s^2\Phi(r) &= g_s^2\rho_s(r) - \frac{m_s^2}{M}\Phi^2(r) \left( \frac{\kappa_3}{2} + \frac{\kappa_4}{3!} \frac{\Phi(r)}{M} \right) \\
&+ \frac{g_s^2}{2M} \left( \eta_1 + \eta_2 \frac{\Phi(r)}{M} \right) \frac{m_\omega^2}{g_\omega^2} W^2(r) + \frac{\eta_\rho}{2M} \frac{g_s^2}{g_\rho^2} m_\rho^2 R^2(r) \\
&+ \frac{\alpha_1}{2M} [(\nabla\Phi(r))^2 + 2\Phi(r)\Delta\Phi(r)] + \frac{\alpha_2}{2M} \frac{g_s^2}{g_\omega^2} (\nabla W(r))^2, \tag{4}
\end{aligned}$$

$$\begin{aligned}
-\Delta W(r) + m_\omega^2 W(r) &= g_\omega^2 \left( \rho(r) + \frac{f_\omega}{2} \rho_T(r) \right) - \left( \eta_1 + \frac{\eta_2}{2} \frac{\Phi(r)}{M} \right) \frac{\Phi(r)}{M} m_\omega^2 W(r) \\
&- \frac{1}{3!} \zeta_0 W^3(r) + \frac{\alpha_2}{M} [\nabla\Phi(r) \cdot \nabla W(r) + \Phi(r)\Delta W(r)] \\
&- 2 \Lambda_\omega g_\omega^2 R^2(r) W(r), \tag{5}
\end{aligned}$$

$$-\Delta R(r) + m_\rho^2 R(r) = \frac{1}{2} g_\rho^2 \left( \rho_3(r) + \frac{1}{2} f_\rho \rho_{T,3}(r) \right) - \eta_\rho \frac{\Phi(r)}{M} m_\rho^2 R(r) - 2 \Lambda_\omega g_\rho^2 R(r) W^2(r), \tag{6}$$

$$-\Delta A(r) = e^2 \rho_p(r), \tag{7}$$

$$-\Delta D(r) + m_\delta^2 D(r) = g_\delta^2 \rho_{s3}, \tag{8}$$

where the baryon, scalar, isovector, proton and tensor densities are

$$\begin{aligned}
\rho(r) &= \sum_\alpha \varphi_\alpha^\dagger(r) \varphi_\alpha(r) \\
&= \rho_p(r) + \rho_n(r) \\
&= \frac{2}{(2\pi)^3} \int_0^{k_p} d^3k + \frac{2}{(2\pi)^3} \int_0^{k_n} d^3k, \tag{9}
\end{aligned}$$

$$\begin{aligned}
\rho_s(r) &= \sum_\alpha \varphi_\alpha^\dagger(r) \beta \varphi_\alpha(r) \\
&= \rho_{sp}(r) + \rho_{sn}(r) \\
&= \sum_\alpha \frac{2}{(2\pi)^3} \int_0^{k_\alpha} d^3k \frac{M_\alpha^*}{(k_\alpha^2 + M_\alpha^{*2})^{\frac{1}{2}}}, \tag{10}
\end{aligned}$$

$$\begin{aligned}
\rho_3(r) &= \sum_\alpha \varphi_\alpha^\dagger(r) \tau_3 \varphi_\alpha(r) \\
&= \rho_p(r) - \rho_n(r), \tag{11}
\end{aligned}$$

$$\begin{aligned}
\rho_{s3}(r) &= \sum_\alpha \varphi_\alpha^\dagger(r) \tau_3 \beta \varphi_\alpha(r) \\
&= \rho_{ps}(r) - \rho_{ns}(r) \tag{12}
\end{aligned}$$

$$\rho_p(r) = \sum_\alpha \varphi_\alpha^\dagger(r) \left( \frac{1 + \tau_3}{2} \right) \varphi_\alpha(r), \tag{13}$$

$$\rho_T(r) = \sum_\alpha \frac{i}{M} \nabla \cdot [\varphi_\alpha^\dagger(r) \beta \alpha \varphi_\alpha(r)], \tag{14}$$

and

$$\rho_{T,3}(r) = \sum_\alpha \frac{i}{M} \nabla \cdot [\varphi_\alpha^\dagger(r) \beta \alpha \tau_3 \varphi_\alpha(r)]. \tag{15}$$

Here  $k_\alpha$  is the nucleon's Fermi momentum and the summation is over all the occupied states. The nucleons and mesons are composite particles and their vacuum polarization effects have been neglected. Hence, the negative-energy states do not contribute to the densities and current [11]. In the fitting process, the coupling constants of the effective Lagrangian are determined from a set of experimental data which takes into account the large part of the vacuum polarization effects in the *no-sea approximation*. It is clear that the *no-sea approximation* is essential to determine the stationary solutions of the relativistic mean-field equations which describe the ground-state properties of the nucleus. The Dirac sea holds the negative energy eigenvectors of the Dirac Hamiltonian which is different for different nuclei. Thus, it depends on the specific solution of the set of nonlinear RMF equations. The Dirac spinors can be expanded in terms of vacuum solutions which form a complete set of plane wave functions in spinor space. This set will be complete when the states with negative energies are the part of the positive energy states and create the Dirac sea of the vacuum.

The effective mass of proton  $M_p^*$  and neutron  $M_n^*$  are written as

$$M_p^* = M - \Phi(r) - D(r), \tag{16}$$

$$M_n^* = M - \Phi(r) + D(r). \quad (17)$$

The vector potential is

$$V(r) = g_\omega V_0(r) + \frac{1}{2} g_\rho \tau_3 b_0(r) + e \frac{(1 - \tau_3)}{2} A_0(r). \quad (18)$$

The set of coupled differential equations are solved self-consistently to describe the ground state properties of finite nuclei. In the fitting procedure, we used the experimental data of binding energy (BE) and charge radius  $r_{ch}$  for a set of spherical nuclei ( $^{16}\text{O}$ ,  $^{40}\text{Ca}$ ,  $^{48}\text{Ca}$ ,  $^{68}\text{Ni}$ ,  $^{90}\text{Zr}$ ,  $^{100,132}\text{Sn}$  and  $^{208}\text{Pb}$ ). The total binding energy is obtained by

$$E_{total} = E_{part} + E_\sigma + E_\omega + E_\rho + E_\delta + E_{\omega\rho} + E_c + E_{pair} + E_{c.m.}, \quad (19)$$

where  $E_{part}$  is the sum of the single particle energies of the nucleons and  $E_\sigma$ ,  $E_\omega$ ,  $E_\rho$ ,  $E_\delta$ ,  $E_c$  are the contributions of the respective mesons and Coulomb fields. The pairing  $E_{pair}$  and the center of mass motion  $E_{cm} = \frac{3}{4} \times 41 A^{-1/3}$  MeV energies are also taken into account [3, 40, 41].

The pairing correlation plays a distinct role in open-shell nuclei [42, 43]. The effect of pairing correlation is markedly seen with the increase in mass number  $A$ . Moreover, it helps in understanding the deformation of medium and heavy nuclei. It has a lean effect on both bulk and single particle properties of lighter mass nuclei because of the availability of limited pairs near the Fermi surface. We take the case of  $T=1$  channel of pairing correlation i.e, pairing between proton- proton and neutron-neutron. The pairs of nucleons are invariant under time reversal symmetry when the pairing interaction  $v_{pair}$  has non-zero matrix elements:

$$\langle \alpha_2 \bar{\alpha}_2 | v_{pair} | \alpha_1 \bar{\alpha}_1 \rangle = -G, \quad (20)$$

where  $\alpha = |nljm\rangle$  and  $\bar{\alpha} = |nlj - m\rangle$  (with  $G > 0$  and  $m > 0$ ) are the quantum states.

A nucleon of quantum states  $|nljm\rangle$  pairs with another nucleon having same  $I_z$  value with quantum states  $|nlj - m\rangle$ , since it is the time reversal partner of the other. In both nuclear and atomic domains, the ideology of BCS pairing is the same. The even-odd mass staggering of isotopes was the first evidence of its kind for the pairing energy. Considering the mean-field formalism the violation of the particle number is seen only due to the pairing correlation. We find terms such as  $\varphi^\dagger \varphi$  (density) in the RMF Lagrangian density but we put an embargo on terms of the form  $\varphi^\dagger \varphi^\dagger$  or  $\varphi \varphi$  since it violates

the particle number conservation. Thus, we affirm that BCS calculations have been carried out by constant gap or constant force approach externally in the RMF model [44–46]. In our work, we consider seniority type interaction as a tool by taking a constant value of  $G$  for pairs of the active pair shell.

The above approach does not go well for nuclei away from the stability line because in the present case, with the increase in the number of neutrons or protons the corresponding Fermi level goes to zero and the number of available levels above it minimizes. To complement this situation we see that the particle-hole and pair excitations reach the continuum. In Ref. [6] we notice that if we make the BCS calculation using the quasiparticle state as in HFB calculation, then the BCS binding energies are coming out to be very close to the HFB, but rms radii (i.e the single-particle wave functions) greatly depend on the size of the box where the calculation is done. This is because of the unphysical neutron (proton) gas in the continuum where wavefunctions are not confined in a region. The above shortcomings of the BCS approach can be improved by means of the so-called quasibound states, i.e, states bound because of their own centrifugal barrier (centrifugal-plus-Coulomb barrier for protons) [3, 47, 48]. Our calculations are done by confining the available space to one harmonic oscillator shell each above and below the Fermi level to exclude the unrealistic pairing of highly excited states in the continuum [3].

## B. Nuclear Matter Properties

### 1. Energy and pressure density

In a static, infinite, uniform and isotropic nuclear matter, all the gradients of the fields in Eqs.(4)-(8) vanish. By the definition of infinite nuclear matter, the electromagnetic interaction is also neglected. The expressions for energy density and pressure for such a system is obtained from the energy-momentum tensor [49]:

$$T_{\mu\nu} = \sum_i \partial_\nu \phi_i \frac{\partial \mathcal{L}}{\partial (\partial^\mu \phi_i)} - g_{\mu\nu} \mathcal{L}. \quad (21)$$

The zeroth component of the energy-momentum tensor  $\langle T_{00} \rangle$  gives the energy density and the third component  $\langle T_{ii} \rangle$  compute the pressure of the system [38]:

$$\begin{aligned}
\mathcal{E} = & \frac{2}{(2\pi)^3} \int d^3k E_i^*(k) + \rho W + \frac{m_s^2 \Phi^2}{g_s^2} \left( \frac{1}{2} + \frac{\kappa_3}{3!} \frac{\Phi}{M} + \frac{\kappa_4}{4!} \frac{\Phi^2}{M^2} \right) \\
& - \frac{1}{2} m_\omega^2 \frac{W^2}{g_\omega^2} \left( 1 + \eta_1 \frac{\Phi}{M} + \frac{\eta_2}{2} \frac{\Phi^2}{M^2} \right) - \frac{1}{4!} \frac{\zeta_0 W^4}{g_\omega^2} + \frac{1}{2} \rho_3 R \\
& - \frac{1}{2} \left( 1 + \frac{\eta_\rho \Phi}{M} \right) \frac{m_\rho^2}{g_\rho^2} R^2 - \Lambda_\omega (R^2 \times W^2) + \frac{1}{2} \frac{m_\delta^2}{g_\delta^2} (D^2), \tag{22}
\end{aligned}$$

$$\begin{aligned}
P = & \frac{2}{3(2\pi)^3} \int d^3k \frac{k^2}{E_i^*(k)} - \frac{m_s^2 \Phi^2}{g_s^2} \left( \frac{1}{2} + \frac{\kappa_3}{3!} \frac{\Phi}{M} + \frac{\kappa_4}{4!} \frac{\Phi^2}{M^2} \right) \\
& + \frac{1}{2} m_\omega^2 \frac{W^2}{g_\omega^2} \left( 1 + \eta_1 \frac{\Phi}{M} + \frac{\eta_2}{2} \frac{\Phi^2}{M^2} \right) + \frac{1}{4!} \frac{\zeta_0 W^4}{g_\omega^2} \\
& + \frac{1}{2} \left( 1 + \frac{\eta_\rho \Phi}{M} \right) \frac{m_\rho^2}{g_\rho^2} R^2 + \Lambda_\omega (R^2 \times W^2) - \frac{1}{2} \frac{m_\delta^2}{g_\delta^2} (D^2), \tag{23}
\end{aligned}$$

where  $E_i^*(k) = \sqrt{k^2 + M_i^{*2}}$  ( $i = p, n$ ) is the energy and  $k$  is the momentum of the nucleon. In the context of density functional theory, it is possible to parametrize the exchange and correlation effects through local potentials (Kohn–Sham potentials), as long as those contributions are small enough [50]. The Hartree values control the dynamics in the relativistic Dirac–Brückner–Hartree–Fock (DBHF) calculations. Therefore, the local meson fields in the RMF formalism can be interpreted as Kohn–Sham potentials and in this sense equations (3–8) include effects beyond the Hartree approach through the non-linear couplings [1].

## 2. Symmetry Energy

The binding energy per nucleon  $\mathcal{E}/A = e(\rho, \alpha)$  can be written in the parabolic form of asymmetry parameter  $\alpha \left( = \frac{\rho_n - \rho_p}{\rho_n + \rho_p} \right)$ :

$$e(\rho, \alpha) = \frac{\mathcal{E}}{\rho_B} - M = e(\rho) + S(\rho)\alpha^2 + \mathcal{O}(\alpha^4), \tag{24}$$

where  $e(\rho)$  is energy density of the symmetric nuclear matter (SNM) ( $\alpha = 0$ ) and  $S(\rho)$  is defined as the symmetry energy of the system:

$$S(\rho) = \frac{1}{2} \left[ \frac{\partial^2 e(\rho, \alpha)}{\partial \alpha^2} \right]_{\alpha=0}. \tag{25}$$

The isospin asymmetry arises due to the difference in densities and masses of the neutron and proton. The density

type isospin asymmetry is taken care by  $\rho$ –meson (isovector–vector meson) and mass asymmetry by  $\delta$ –meson (isovector–scalar meson). The general expression for symmetry energy  $S(\rho)$  is a combined expression of  $\rho$ – and  $\delta$ –mesons, which is defined as [3, 20, 51, 52]:

$$S(\rho) = S^{kin}(\rho) + S^\rho(\rho) + S^\delta(\rho), \tag{26}$$

with

$$S^{kin}(\rho) = \frac{k_F^2}{6E_F^*}, \quad S^\rho(\rho) = \frac{g_\rho^2 \rho}{8m_\rho^{*2}} \tag{27}$$

and

$$S^\delta(\rho) = -\frac{1}{2} \rho \frac{g_\delta^2}{m_\delta^2} \left( \frac{M^*}{E_F} \right)^2 u_\delta(\rho, M^*). \tag{28}$$

The last function  $u_\delta$  is from the discreteness of the Fermi momentum. This momentum is quite large in nuclear matter and can be treated as a continuum and continuous system. The function  $u_\delta$  is defined as:

$$u_\delta(\rho, M^*) = \frac{1}{1 + 3 \frac{g_\delta^2}{m_\delta^2} \left( \frac{\rho^s}{M^*} - \frac{\rho}{E_F} \right)}. \tag{29}$$

In the limit of continuum, the function  $u_\delta \approx 1$ . The whole symmetry energy ( $S^{kin} + S^{pot}$ ) arises from  $\rho$ – and  $\delta$ –mesons is given as:

$$S(\rho) = \frac{k_F^2}{6E_F^*} + \frac{g_\rho^2 \rho}{8m_\rho^{*2}} - \frac{1}{2} \rho \frac{g_\delta^2}{m_\delta^2} \left( \frac{M^*}{E_F} \right)^2, \tag{30}$$

where  $E_F^*$  is the Fermi energy and  $k_F$  is the Fermi momentum. The mass of the  $\rho$ -meson modified, because of the cross-coupling of  $\rho - \omega$  fields and is given by

$$m_\rho^{*2} = \left(1 + \eta_\rho \frac{\Phi}{M}\right) m_\rho^2 + 2g_\rho^2(\Lambda_\omega W^2). \quad (31)$$

The cross-coupling of isoscalar-isovector mesons ( $\Lambda_\omega$ ) modifies the density dependence of  $S(\rho)$  without affecting the saturation properties of the symmetric nuclear matter (SNM) [26, 53, 54]. In the numerical calculation, the coefficient of symmetry energy  $S(\rho)$  is obtained by the energy difference of symmetric and pure neutron matter at saturation. In our calculation, we have taken the isovector channel into account to make the new parameters, which incorporate the currently existing experimental observations and predictions are done keeping in mind some future aspects of the model. The symmetry energy can be expanded as a Taylor series around the saturation density  $\rho_0$  as:

$$S(\rho) = J + L\mathcal{Y} + \frac{1}{2}K_{sym}\mathcal{Y}^2 + \frac{1}{6}Q_{sym}\mathcal{Y}^3 + \mathcal{O}[\mathcal{Y}^4], \quad (32)$$

where  $J = S(\rho_0)$  is the symmetry energy at saturation and  $\mathcal{Y} = \frac{\rho - \rho_0}{3\rho_0}$ . The coefficients  $L(\rho_0)$ ,  $K_{sym}(\rho_0)$ , and  $Q_{sym}$  are defined as:

$$L = 3\rho \left. \frac{\partial S(\rho)}{\partial \rho} \right|_{\rho=\rho_0}, \quad (33)$$

$$K_{sym} = 9\rho^2 \left. \frac{\partial^2 S(\rho)}{\partial \rho^2} \right|_{\rho=\rho_0=0}, \quad (34)$$

$$Q_{sym} = 27\rho^3 \left. \frac{\partial^3 S(\rho)}{\partial \rho^3} \right|_{\rho=\rho_0=0}. \quad (35)$$

Similarly, we obtain the asymmetric nuclear matter (ANM) incompressibility as  $K(\alpha) = K + K_\tau \alpha^2 + \mathcal{O}(\alpha^4)$  and  $K_\tau$  is given by [55]

$$K_\tau = K_{sym} - 6L - \frac{Q_0 L}{K}, \quad (36)$$

where  $Q_0 = 27\rho^3 \frac{\partial^3(\mathcal{E}/\rho)}{\partial \rho^3}$  in SNM.

Here,  $L$  is the slope and  $K_{sym}$  represents the curvature of  $S(\rho)$  at saturation density. A large number of investigations have been made to fix the values of  $J$ ,  $L$  and  $K_{sym}$  [53, 56–61]. The density dependence of symmetry energy is a key quantity to control the properties of both finite nuclei and infinite nuclear matter [62]. Currently, the available information on symmetry energy  $J = 31.6 \pm 2.66$  MeV and its slope  $L = 58.9 \pm 16$  MeV at saturation density are obtained by various astrophysical observations [63]. Till date, the precise values of  $J$ ,  $L$  and the neutron radii for finite nuclei are not known experimentally, it is essential to discuss the behavior of the symmetry energy as a function of density in our new parameter set.

### III. PARAMETER FITTING

The simulated annealing method (SAM) is used to determine the parameters used in the Lagrangian density [64, 65]. The SAM is useful in the global minimization technique, *i.e.*, it gives accurate results when there exists a global minimum within several local minima. Usually, this procedure is used in a system when the number of parameters are more than the observables [66–68]. In this simulation method, the system stabilizes, when the temperature  $T$  (a variable which controls the energy of the system) goes down [33–35]. Initially, the nuclear system is put at a high temperature (highly unstable) and then allowed to cool down slowly so that it is stabilized in a very smooth way and finally reaches the frozen temperature (stable or systematic system). The variation of  $T$  should be very small near the stable state. The  $\chi^2 = \chi^2(p_1, \dots, p_N)$  values of the considered systems are minimized (least-square fit), which is governed by the model parameters  $p_i$ . The general expression of the  $\chi^2$  can be given as:

$$\chi^2 = \frac{1}{N_d - N_p} \sum_{i=1}^{N_d} \left( \frac{M_i^{exp} - M_i^{th}}{\sigma_i} \right)^2. \quad (37)$$

Here,  $N_d$  and  $N_p$  are the number of experimental data points and the fitting parameters, respectively. The experimental and theoretical values of the observables are denoted by  $M_i^{exp}$  and  $M_i^{th}$ , respectively. The  $\sigma_i$ 's are the adopted errors [69]. The adopted errors are composed of three components, namely, the experimental, numerical and theoretical errors [69]. As the name suggests, the experimental errors are associated with the measurements, numerical and the theoretical errors are associated with the numerics and the shortcomings of the nuclear model employed, respectively. In principle, there exists some arbitrariness in choosing the values of  $\sigma_i$  which is partially responsible for the proliferation of the mean-field models. Only guidance available from the statistical analysis is that the chi-square per degree of freedom (Eq. 37) should be close to the unity. In the present calculation, we have used some selected fit data for binding energy and root mean square radius of charge distribution for some selected nuclei and the associated adopted errors on them [70].

In our calculations, we have built a new parameter set IOPB-I and analyzed their effects for finite and infinite nuclear systems. Thus, we performed an overall fit with 8 parameters, where the nucleons as well as the masses of the two vector mesons in free space are fixed at their experimental values *i.e.*,  $M = 939$  MeV,  $m_\omega = 782.5$  MeV and  $m_\rho = 763.0$  MeV. The effective nucleon mass can be used as a nuclear matter constraint at the saturation density  $\rho_0$  along with other empirical values like incompressibility, binding energy per nucleon and asymmetric parameter  $J$ . While fitting the parameter, the value of effective nucleon mass  $M^*/M$ , nuclear matter incompressibility  $K$  and symmetry energy coefficient  $J$  are constrained within 0.50-0.90, 220-260 MeV and 28-36 MeV, respectively. The minimum  $\chi^2$  is obtained by simulated annealing method [33–35] to fix the final parameters. The newly developed IOPB-I set along with NL3 [13], FSUGar-

TABLE I: The obtained new parameter set IOPB-I along with NL3 [13], FSUGarnet [71] and G3 [21] sets are listed. The nucleon mass  $M$  is 939.0 MeV. All the coupling constants are dimensionless, except  $k_3$  which is in  $\text{fm}^{-1}$ .

	NL3	FSUGarnet	G3	IOPB-I
$m_s/M$	0.541	0.529	0.559	0.533
$m_\omega/M$	0.833	0.833	0.832	0.833
$m_\rho/M$	0.812	0.812	0.820	0.812
$m_\delta/M$	0.0	0.0	1.043	0.0
$g_s/4\pi$	0.813	0.837	0.782	0.827
$g_\omega/4\pi$	1.024	1.091	0.923	1.062
$g_\rho/4\pi$	0.712	1.105	0.962	0.885
$g_\delta/4\pi$	0.0	0.0	0.160	0.0
$k_3$	1.465	1.368	2.606	1.496
$k_4$	-5.688	-1.397	1.694	-2.932
$\zeta_0$	0.0	4.410	1.010	3.103
$\eta_1$	0.0	0.0	0.424	0.0
$\eta_2$	0.0	0.0	0.114	0.0
$\eta_\rho$	0.0	0.0	0.645	0.0
$\Lambda_\omega$	0.0	0.043	0.038	0.024
$\alpha_1$	0.0	0.0	2.000	0.0
$\alpha_2$	0.0	0.0	-1.468	0.0
$f_\omega/4$	0.0	0.0	0.220	0.0
$f_\rho/4$	0.0	0.0	1.239	0.0
$\beta_\sigma$	0.0	0.0	-0.087	0.0
$\beta_\omega$	0.0	0.0	-0.484	0.0

net [71] and G3 [21] are given for comparison in Table I. The calculated results of the binding energy and charge radius are compared with the known experimental data [72, 73]. It is to be noted that in the original E-RMF parametrization, only five spherical nuclei were taken into consideration while fitting the parameters with the binding energy, charge radius and single particle energy [1]. However, here, eight spherical nuclei are used for the fitting as listed in Table II.

#### IV. RESULTS AND DISCUSSIONS

In this section we discuss our calculated results for finite nuclei, infinite nuclear matter and neutron stars. For finite nuclei, binding energy, rms radii for neutron and proton distributions, two neutron separation energy and neutron-skin thickness are analyzed. Similarly, for infinite nuclear matter system, the binding energy per particle for symmetric and asymmetric nuclear matter including pure neutron matter at both sub-saturation and supra-saturation densities are compared with other theoretical results and experimental data. The parameter set IOPB-I is also applied to study the structure of neutron star using  $\beta$ -equilibrium and charge neutrality conditions.

TABLE II: The calculated binding energy per particle (B/A) and charge radius ( $R_c$ ) are compared with the available experimental data [72, 73]. The predicted neutron-skin thickness  $\Delta r_{np} = R_n - R_p$  is also depicted with all the four models.

Nucleus	Obs.	Expt.	NL3	FSUGarnet	G3	IOPB-I
$^{16}\text{O}$	B/A	7.976	7.917	7.876	8.037	7.977
	$R_c$	2.699	2.714	2.690	2.707	2.705
	$R_n-R_p$	-	-0.026	-0.028	-0.028	-0.027
$^{40}\text{Ca}$	B/A	8.551	8.540	8.528	8.561	8.577
	$R_c$	3.478	3.466	3.438	3.459	3.458
	$R_n-R_p$	-	-0.046	-0.051	-0.049	-0.049
$^{48}\text{Ca}$	B/A	8.666	8.636	8.609	8.671	8.638
	$R_c$	3.477	3.443	3.426	3.466	3.446
	$R_n-R_p$	-	0.229	0.169	0.174	0.202
$^{68}\text{Ni}$	B/A	8.682	8.698	8.692	8.690	8.707
	$R_c$	-	3.870	3.861	3.892	3.873
	$R_n-R_p$	-	0.262	0.184	0.190	0.223
$^{90}\text{Zr}$	B/A	8.709	8.695	8.693	8.699	8.691
	$R_c$	4.269	4.253	4.231	4.276	4.253
	$R_n-R_p$	-	0.115	0.065	0.068	0.091
$^{100}\text{Sn}$	B/A	8.258	8.301	8.298	8.266	8.284
	$R_c$	-	4.469	4.426	4.497	4.464
	$R_n-R_p$	-	-0.073	-0.078	-0.079	-0.077
$^{132}\text{Sn}$	B/A	8.355	8.371	8.372	8.359	8.352
	$R_c$	4.709	4.697	4.687	4.732	4.706
	$R_n-R_p$	-	0.349	0.224	0.243	0.287
$^{208}\text{Pb}$	B/A	7.867	7.885	7.902	7.863	7.870
	$R_c$	5.501	5.509	5.496	5.541	5.521
	$R_n-R_p$	-	0.283	0.162	0.180	0.221

TABLE III: The nuclear matter properties such as binding energy per nucleon  $\mathcal{E}_0(\text{MeV})$ , saturation density  $\rho_0(\text{fm}^{-3})$ , incompressibility coefficient for symmetric nuclear matter  $K(\text{MeV})$ , effective mass ratio  $M^*/M$ , symmetry energy  $J(\text{MeV})$  and linear density dependence of the symmetry energy  $L(\text{MeV})$  at saturation.

	NL3	FSUGarnet	G3	IOPB-I
$\rho_0(\text{fm}^{-3})$	0.148	0.153	0.148	0.149
$\mathcal{E}_0(\text{MeV})$	-16.29	-16.23	-16.02	-16.10
$M^*/M$	0.595	0.578	0.699	0.593
$J(\text{MeV})$	37.43	30.95	31.84	33.30
$L(\text{MeV})$	118.65	51.04	49.31	63.58
$K_{sym}(\text{MeV})$	101.34	59.36	-106.07	-37.09
$Q_{sym}(\text{MeV})$	177.90	130.93	915.47	862.70
$K(\text{MeV})$	271.38	229.5	243.96	222.65
$Q_0(\text{MeV})$	211.94	15.76	-466.61	-101.37
$K_\tau(\text{MeV})$	-703.23	-250.41	-307.65	-389.46
$K_{asy}(\text{MeV})$	-610.56	-246.89	-401.97	-418.58
$K_{sat2}(\text{MeV})$	-703.23	-250.41	-307.65	-389.46

TABLE IV: The binary neutron star masses ( $m_1(M_\odot), m_2(M_\odot)$ ) and corresponding radii ( $R_1(\text{km}), R_2(\text{km})$ ), tidal love number ( $(k_2)_1, (k_2)_2$ ), tidal deformabilities ( $\lambda_1, \lambda_2$ ) in  $10^{36} \text{g cm}^2 \text{s}^2$  and dimensionless tidal deformabilities ( $\Lambda_1, \Lambda_2$ ).  $\tilde{\Lambda}, \delta\tilde{\Lambda}, \mathcal{M}_c(M_\odot)$  and  $\mathcal{R}_c(\text{km})$  are the dimensionless tidal deformability, tidal correction, chirp mass and radius of the binary neutron star, respectively.

EoS	$m_1(M_\odot)$	$m_2(M_\odot)$	$R_1(\text{km})$	$R_2(\text{km})$	$(k_2)_1$	$(k_2)_2$	$\lambda_1$	$\lambda_2$	$\Lambda_1$	$\Lambda_2$	$\tilde{\Lambda}$	$\delta\tilde{\Lambda}$	$\mathcal{M}_c(M_\odot)$	$\mathcal{R}_c(\text{km})$
NL3	1.20	1.20	14.702	14.702	0.1139	0.1139	7.826	7.826	2983.15	2983.15	2983.15	0.000	1.04	10.350
	1.50	1.20	14.736	14.702	0.0991	0.1139	6.889	7.826	854.06	2983.15	1608.40	220.223	1.17	10.214
	1.25	1.25	14.708	14.708	0.1118	0.1118	7.962	7.962	2388.82	2388.82	2388.82	0.000	1.09	10.313
	1.30	1.30	14.714	14.714	0.1094	0.1094	7.546	7.546	1923.71	1923.71	1923.71	0.000	1.13	10.271
	1.35	1.35	14.720	14.720	0.1070	0.1070	7.393	7.393	1556.84	1556.84	1556.84	0.000	1.18	10.224
	1.35	1.25	14.720	14.708	0.1070	0.1118	7.393	7.962	1556.84	2388.82	1930.02	91.752	1.13	10.268
	1.37	1.25	14.722	14.708	0.1061	0.1118	7.339	7.962	1452.81	2388.82	1863.78	100.532	1.14	10.271
	1.40	1.20	14.726	14.702	0.1044	0.1139	7.231	7.826	1267.07	2983.15	1950.08	183.662	1.13	10.262
	1.40	1.40	14.726	14.726	0.1044	0.1044	7.231	7.231	1267.07	1267.07	1267.07	0.000	1.22	10.174
	1.42	1.29	14.728	14.712	0.1031	0.1099	7.147	7.572	1145.72	1994.02	1515.18	95.968	1.18	10.192
	1.44	1.39	14.730	14.724	0.1027	0.1049	7.120	7.259	1108.00	1311.00	1204.83	19.212	1.23	10.179
	1.45	1.45	14.732	14.732	0.1018	0.1018	7.064	7.064	1037.13	1037.13	1037.13	0.000	1.26	10.124
	1.54	1.26	14.740	14.708	0.0969	0.1114	6.741	7.668	729.95	2303.95	1308.91	168.202	1.21	10.179
	1.60	1.60	14.746	14.746	0.0937	0.0937	6.532	6.532	589.92	589.92	589.92	0.000	1.39	9.979
	FSUGarnet	1.20	1.20	12.944	12.944	0.1090	0.1090	3.961	3.961	1469.32	1469.32	1469.32	0.000	1.04
1.50		1.20	12.972	12.944	0.0893	0.1090	3.282	3.961	408.91	1469.32	784.09	111.643	1.17	8.847
1.25		1.25	12.958	12.958	0.1062	0.1062	3.880	3.880	1193.78	1193.78	1193.78	0.000	1.09	8.977
1.30		1.30	12.968	12.968	0.1030	0.1030	3.777	3.777	945.29	945.29	945.29	0.000	1.13	8.910
1.35		1.35	12.974	12.974	0.0998	0.0998	3.666	3.666	761.13	761.13	761.13	0.000	1.18	8.860
1.35		1.25	12.974	12.958	0.0998	0.1062	3.666	3.880	761.13	1193.78	955.00	49.744	1.13	8.920
1.37		1.25	12.976	12.958	0.0986	0.1062	3.629	3.880	710.62	1193.78	922.54	53.853	1.14	8.924
1.40		1.20	12.978	12.944	0.0965	0.1090	3.552	3.961	622.06	1469.32	959.22	90.970	1.13	8.904
1.40		1.40	12.978	12.978	0.0965	0.0965	3.552	3.552	622.06	622.06	622.06	0.000	1.22	8.825
1.42		1.29	12.978	12.966	0.0949	0.1038	3.495	3.803	565.47	1001.18	755.10	50.492	1.18	8.867
1.44		1.39	12.978	12.978	0.0939	0.0973	3.456	3.582	531.54	653.60	589.65	14.148	1.23	8.823
1.45		1.45	12.978	12.978	0.0931	0.0931	3.427	3.427	507.70	507.70	507.70	0.000	1.26	8.776
1.54		1.26	12.964	12.960	0.0862	0.1057	3.157	3.864	343.73	1146.73	638.35	88.892	1.21	8.817
1.60		1.60	12.944	12.944	0.0816	0.0816	2.964	2.964	266.20	266.20	266.20	0.000	1.39	8.511
G3		1.20	1.20	12.466	12.466	0.1034	0.1034	3.114	3.114	1776.65	1776.65	1776.65	0.000	1.04
	1.50	1.20	112.360	12.466	0.0800	0.1034	2.309	3.114	284.92	1776.65	803.43	191.605	1.17	8.890
	1.25	1.25	12.460	12.460	0.1001	0.1001	3.007	3.007	939.79	939.79	939.79	0.000	1.09	8.557
	1.30	1.30	12.448	12.448	0.0962	0.0962	2.875	2.875	728.07	728.07	728.07	0.000	1.13	8.457
	1.35	1.35	12.434	12.434	0.0925	0.0925	2.750	2.750	582.26	582.26	582.26	0.000	1.18	8.398
	1.35	1.25	12.434	12.460	0.0925	0.1001	2.750	3.007	582.26	939.79	742.29	43.064	1.13	8.482
	1.37	1.25	12.428	12.460	0.0909	0.1001	2.696	3.007	530.66	939.79	709.72	49.144	1.14	8.468
	1.40	1.20	12.416	12.466	0.0859	0.1034	2.613	3.114	461.03	1776.65	976.80	183.274	1.13	8.937
	1.40	1.40	12.416	12.416	0.0859	0.0859	2.613	2.613	461.03	461.03	461.03	0.000	1.22	8.312
	1.42	1.29	12.408	12.450	0.0868	0.0972	2.553	2.905	417.96	772.17	571.87	43.226	1.18	8.387
	1.44	1.39	12.398	12.420	0.0854	0.0894	2.501	2.643	384.42	484.90	432.22	12.671	1.23	8.292
	1.45	1.45	12.932	12.392	0.0846	0.0846	2.472	2.472	367.04	367.04	367.04	0.000	1.26	8.225
	1.54	1.26	12.334	12.458	0.0769	0.0992	2.194	2.976	239.49	883.46	474.83	75.175	1.21	8.311
	1.60	1.60	12.280	12.280	0.0716	0.0716	2.000	2.000	179.63	179.63	179.63	0.000	1.39	7.867

TABLE V: Table IV is continued ...

EoS	$m_1(M_\odot)$	$m_2(M_\odot)$	$R_1(\text{km})$	$R_2(\text{km})$	$(k_2)_1$	$(k_2)_2$	$\lambda_1$	$\lambda_2$	$\Lambda_1$	$\Lambda_2$	$\bar{\Lambda}$	$\delta\bar{\Lambda}$	$\mathcal{M}_c(M_\odot)$	$\mathcal{R}_c(\text{km})$
IOPB-I	1.20	1.20	13.222	13.222	0.1081	0.1081	4.369	4.369	1654.23	1654.23	1654.23	0.000	1.04	9.199
	1.50	1.20	13.236	13.222	0.0894	0.1081	3.631	4.369	449.62	1654.23	875.35	128.596	1.17	9.044
	1.25	1.25	13.230	13.230	0.1053	0.1053	4.268	4.268	1310.64	1310.64	1310.64	0.000	1.09	9.146
	1.30	1.30	13.238	13.238	0.1024	0.1024	4.162	4.162	1053.07	1053.07	1053.07	0.000	1.13	9.105
	1.35	1.35	13.240	13.240	0.0995	0.0995	4.050	4.050	857.53	857.53	857.53	0.000	1.18	9.074
	1.35	1.25	13.240	13.230	0.0995	0.1053	4.050	4.268	857.53	1310.64	1060.81	49.565	1.13	9.110
	1.37	1.25	13.242	13.230	0.0938	0.1053	4.004	4.268	791.92	1310.64	1019.60	56.371	1.14	9.104
	1.40	1.20	13.242	13.222	0.0960	0.1081	3.911	4.369	680.79	1654.23	1067.64	107.340	1.13	9.097
	1.40	1.40	13.242	13.242	0.0960	0.0960	3.911	3.911	680.79	680.79	680.79	0.000	1.22	8.986
	1.42	1.29	13.242	13.236	0.0949	0.1030	3.864	4.184	632.31	1099.78	835.91	52.836	1.18	9.049
	1.44	1.39	13.242	13.242	0.0935	0.0969	3.806	3.946	578.47	719.80	645.73	17.094	1.23	8.985
	1.45	1.45	13.240	13.240	0.0927	0.0927	3.771	3.771	549.06	549.06	549.06	0.000	1.26	8.915
	1.54	1.26	13.230	13.232	0.0868	0.1047	3.516	4.247	384.65	1253.00	703.58	94.735	1.21	8.991
	1.60	1.60	13.212	12.212	0.0823	0.0823	3.314	3.314	296.81	296.81	296.81	0.000	1.39	8.698

## A. FINITE NUCLEI

### (i) Binding energies, charge radii and neutron-skin thickness

We have used eight spherical nuclei to fit the experimental ground-state binding energies and charge radii using SAM. The calculated results are listed in Table II and compared with other theoretical models as well as experimental data [72, 73]. It can be seen that the NL3 [13], FSUGarnet [71]

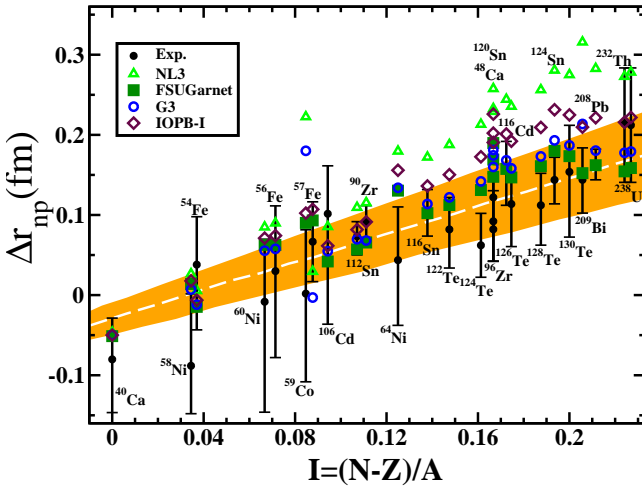


FIG. 1: (color online) The neutron-skin thickness as a function of the asymmetry parameter. Results obtained with the parameter set IOPB-I are compared with those of the set NL3 [13], FSUGarnet [71], G3 [21] and experimental values [74]. The shaded region is calculated using Eq.39.

and G3 [21] successfully reproduce the energies and charge radii as well. Although, the "mean-field models are not expected to work well for the light nuclei" but the results deviate only marginally for the ground state properties for light nuclei [75]. We noticed that both the binding energy and charge radii of  $^{16}\text{O}$  are well produced by IOPB-I. However, the charge radii of  $^{40,48}\text{Ca}$  slightly underestimate the data. We would like to emphasize that it is an open problem to mean-field models to predict the evolution of charge radii of  $^{38-52}\text{Ca}$  (see Fig. 3 in Ref. [76]).

The excess of neutrons give rise to a neutron-skin thickness. The neutron-skin thickness  $\Delta r_{np}$  is defined as

$$\Delta r_{np} = \langle r^2 \rangle_n^{1/2} - \langle r^2 \rangle_p^{1/2} = R_n - R_p. \quad (38)$$

with  $R_n$  and  $R_p$  being the rms radii for the neutron and proton distributions, respectively. The  $\Delta r_{np}$ , strongly correlated with the slope of the symmetry energy [77–79], can probe isovector part of the nuclear interaction. However, there is a large uncertainty in the experimental measurement of neutron distribution radius of the finite nuclei. The current values of neutron radius and neutron-skin thickness of  $^{208}\text{Pb}$  are  $5.78^{+0.16}_{-0.18}$  and  $0.33^{+0.16}_{-0.18}$  fm, respectively [80]. This error bar is too large to provide significant constraints on the density-dependent of symmetry energy. It is expected that PREX-II result will give us the neutron radius of  $^{208}\text{Pb}$  within 1% accuracy. The inclusion of some isovector dependent terms in the Lagrangian density is needed which would provide the freedom to refit the coupling constants within the experimental data without compromising the quality of fit. The addition of  $\omega - \rho$  cross-coupling into the Lagrangian density controls the neutron-skin thickness of  $^{208}\text{Pb}$  as well as for other nuclei. In Fig. 1, we show neutron-skin thickness  $\Delta r_{np}$  for  $^{40}\text{Ca}$  to  $^{238}\text{U}$  nuclei as a function of proton-neutron asymmetry  $I = (N - Z)/A$ . The calculated results of  $\Delta r_{np}$  for NL3, FSUGarnet, G3 and IOPB-I parameter sets are compared with the corresponding

experimental data [74]. Experiments have been done with antiprotons at CERN and the  $\Delta r_{np}$  are extracted for 26 stable nuclei ranging from  $^{40}\text{Ca}$  to  $^{238}\text{U}$  as displayed in the figure along with the error bars. The trend of the data points show approximately linear dependence of neutron-skin thickness on the relative neutron excess  $I$  of nucleus that can be fitted by [74, 81]:

$$\Delta r_{np} = (0.90 \pm 0.15)I + (-0.03 \pm 0.02) \text{ fm}. \quad (39)$$

The values of  $\Delta r_{np}$  obtained with IOPB-I for some of the nuclei slightly deviate from the shaded region as can be seen from Fig. 1. This is because, IOPB-I has a smaller strength of  $\omega - \rho$  cross-coupling as compared to FSUGarnet. Recently, F. Fattoyev *et al.* constraint the upper limit of  $\Delta r_{np} \lesssim 0.25$  fm for  $^{208}\text{Pb}$  nucleus with the help of GW170817 observation data [82]. The calculated values of neutron-skin thickness for

the  $^{208}\text{Pb}$  nucleus are 0.283, 0.162, 0.180 and 0.221 fm for the NL3, FSUGarnet, G3 and IOPB-I parameter sets respectively. The proton elastic scattering experiment has recently measured neutron-skin thickness  $\Delta r_{np} = 0.211^{+0.054}_{-0.063}$  fm for  $^{208}\text{Pb}$  [84]. Thus values of  $\Delta r_{np} = 0.221$  for IOPB-I are consistent with recent prediction of neutron-skin thickness.

## (ii) Two-neutron separation energy $S_{2n}(Z, N)$

The large shell gap in single particle energy levels is an indication of the magic number. This is responsible for the extra stability for the magic nuclei. The extra stability for a particular nucleon number can be understood from the sudden fall in the two-neutron separation energy  $S_{2n}$ . The  $S_{2n}$  can be estimated by the difference in ground state binding energies of two isotopes *i.e.*,

$$S_{2n}(Z, N) = BE(Z, N) - BE(Z, N - 2). \quad (40)$$

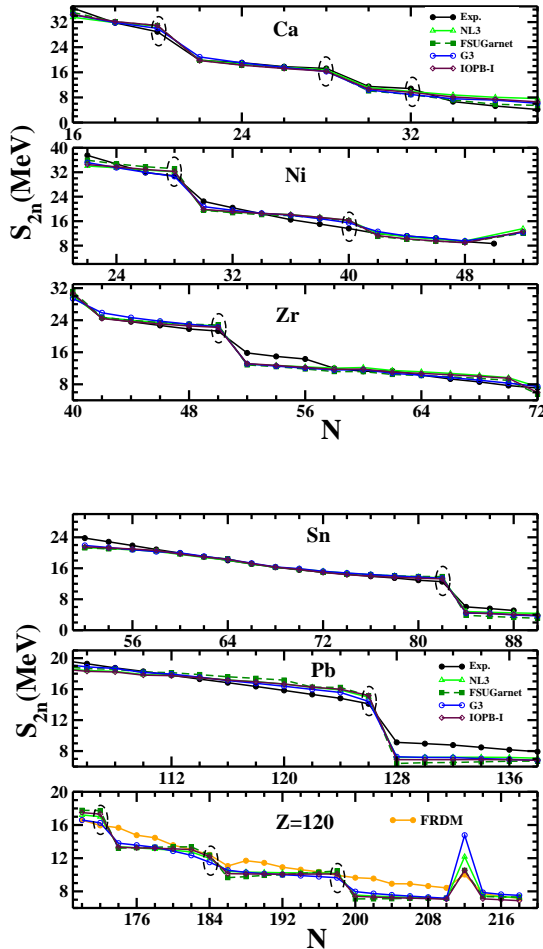


FIG. 2: (color online) The two-neutron separation energy as a function of neutron number for the isotopic series of Ca, Ni, Zr, Sn and Pb nuclei with NL3 [13], FSUGarnet [71], G3 [21], FRDM [83] and experimental data [72] whenever available. The dotted circle represents the magicity of the nuclei.

In Fig. 2, we display results for the  $S_{2n}$  as a function of neutron numbers for Ca, Ni, Zr, Sn, Pb and  $Z=120$  isotopic chains. The calculated results are compared with the finite range droplet model (FRDM) [83] and latest experimental data [72]. From the figure, it is clear that there is an evolution of magicity as one moves from the valley of stability to the *drip-line*. In all cases, the  $S_{2n}$  values decrease gradually with increase in neutron number. The experimental manifestation of large shell gaps at neutron number  $N = 20, 28(\text{Ca}), 28(\text{Ni}), 50(\text{Zr}), 82(\text{Sn})$  and  $126(\text{Pb})$  are reasonably well reproduced by the four relativistic sets. Figure 2 shows that the experimental  $S_{2n}$  of  $^{50-52}\text{Ca}$  are in good agreement with the prediction of NL3 set. It is interesting to note that all sets predict the sub-shell closure at  $N=40$  for Ni isotopes. Furthermore, the two-neutron separation energy for the isotopic chain of nuclei with  $Z=120$  is also displayed in Fig. 2. For the isotopic chain of  $Z=120$ , no experimental information exist. The only comparison can be made with theoretical models such as the FRDM [72]. At  $N=172, 184$  and  $198$  sharp falls in separation energy is seen for all forces, which have been predicted by various theoretical models in the superheavy mass region [85–88]. It is to be noted that the isotopes with  $Z=120$  are shown to be spherical in their ground state [88]. In a detail calculation, Bhuyan and Patra using both RMF and Skyrme-Hartree-Fock formalisms, predicted that  $Z=120$  could be the next magic number after  $Z=82$  in the superheavy region [89]. Thus, the deformation effects may not affect the results for  $Z=120$ . Therefore, a future mass measurement of  $^{292,304,318}120$  would confirm a key test for the theory, as well as direct information about the closed-shell behavior at  $N=172, 184$  and  $198$ .

## B. Infinite Nuclear Matter

The nuclear incompressibility  $K$  determines the extent to which the nuclear matter can be compressed. This plays important role in the nuclear equation of state (EoS). Currently,

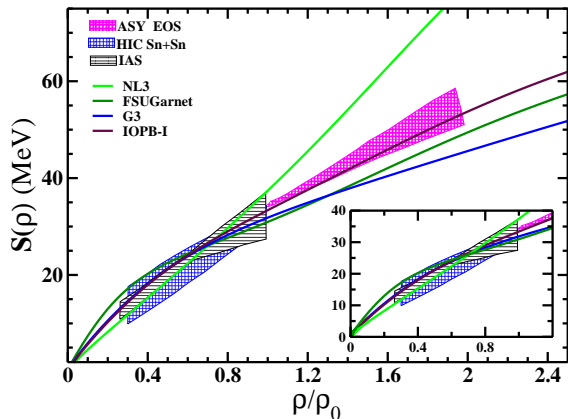


FIG. 3: (color online) Density dependent symmetry energy from Eq. (32) with different E-RMF parameter sets along with IOPB-I parametrization. The shaded region is the symmetry energy from IAS [90], HIC Sn+Sn [91] and ASY-EoS experimental data [92]. The zoomed pattern of the symmetry energy at low densities is shown in the inset.

the accepted value of  $K = 240 \pm 20$  MeV has been determined from isoscalar giant monopole resonance (ISGMR) for  $^{90}\text{Zr}$  and  $^{208}\text{Pb}$  nuclei [93, 94]. For our parameter set IOPB-I, we get  $K = 222.65$  MeV. The density-dependent symmetry energy  $S(\rho)$  is determined from Eq.(32) using IOPB-I along with three adopted models. The calculated results of the symmetry energy coefficient ( $J$ ), the slope of symmetry energy ( $L$ ) and other saturation properties are listed in Table III. We find that in case of IOPB-I,  $J = 33.3$  MeV and  $L = 63.6$  MeV. These values are compatible with  $J = 31.6 \pm 2.66$  MeV and  $L = 58.9 \pm 16$  MeV obtained by various terrestrial experimental informations and astrophysical observations [63].

Another important constraint  $K_\tau$  has been suggested which lies in the range of -840 MeV to -350 MeV [95–97] by various experimental data on isoscalar giant monopole resonance, which we can calculate from Eq.(36). It is to be noticed that the calculated values of  $K_\tau$  are -703.23, -250.41, -307.65 and -389.46 MeV for NL3, FSUGarnet, G3 and IOPB-I parameter sets, respectively. The ISGMR measurement has been investigated in a series of  $^{112-124}\text{Sn}$  isotopes, which extracted the value of  $K_\tau = -395 \pm 40$  MeV [98]. It is found that  $K_\tau = -389.46$  MeV for IOPB-I set is consistent with GMR measurement [98]. In the absence of cross-coupling,  $S(\rho)$  of NL3 is stiffer at low and high-density regime as displayed in Fig. 3. Alternatively, presence of cross-coupling of  $\rho$  mesons to the  $\omega$  (in case of FSUGarnet and IOPB-I) and  $\sigma$  mesons (in case of G3) yields the softer symmetry energy at low-density which are consistent with HIC Sn+Sn [91], IAS [90] data as shown in the figure. However, IOPB-I has softer  $S(\rho)$  in comparison to NL3 parameter set at higher density which lies inside the shaded region of ASY-EoS experimental data [92].

Next, we display in Fig. 4 the binding energy per neutron ( $B/N$ ) as a function of the neutron density. Here, special at-

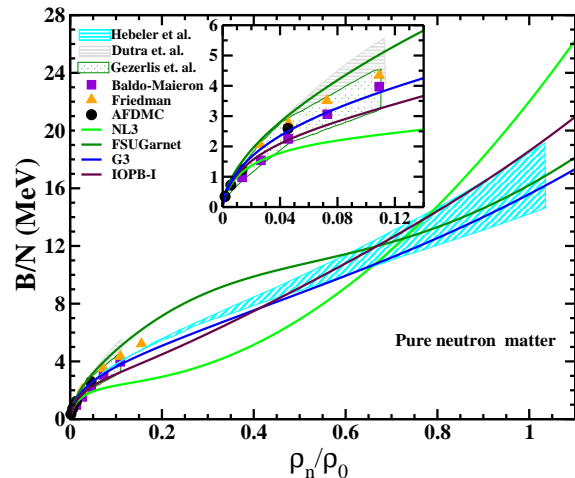


FIG. 4: (color online) The energy per neutron as a function of neutron density with NL3 [13], FSUGarnet [71], G3 [21] and IOPB-I parameter sets. Other curves and shaded region represents the results for various microscopic approaches such as Baldo-Maieron [99], Friedman [100], Auxiliary-field diffusion Monte Carlo [101], Dutra [57], Gezerlis [102] and Hebeler [103].

tention is needed to build nucleon-nucleon interaction to fit the data at sub-saturation density. For example, the EoS of pure neutron matter (PNM) at low density obtained within the variational method, which is obtained with a Urbana  $v_{14}$  interaction [100]. In this regard, the effective mean field models also fulfill this demand to some extent [21, 71, 104]. The cross-coupling  $\omega - \rho$  plays an important role at low-density of the PNM. The low-density (zoomed pattern) nature of the FSUGarnet, G3 and IOPB-I are in harmony with the results obtained by microscopic calculations [57, 99–102], while the results for NL3 deviate from the shaded region at low as well as high density regions. We also find a very good agreement for FSUGarnet, G3 and IOPB-I at higher densities, which have been obtained with chiral NN and 3N interactions [103].

In Fig. 5, we show the calculated pressure  $P$  for the symmetric nuclear matter (SNM) and PNM with the baryon density for the four E-RMF models and then are compared with the experimental flow data [105]. It is seen from Fig. 5(a) that the SNM EoS for G3 parameter set is in excellent agreement with the flow data for the entire density range. The SNM EoSs for the FSUGarnet and IOPB-I are also compatible with the experimental HIC data but they are stiffer relative to the EoS for the G3 parameterization. In Fig. 5(b), the bounds on the PNM equation of states (EoSs) are divided into two categories (i) the upper one corresponds to a strong density dependence of symmetry energy  $S(\rho)$  (HIC-Asy Stiff) and (ii) the lower one corresponds to the weakest  $S(\rho)$  (HIC-Asy Soft) [105, 106]. Our parameter set IOPB-I along with G3 and FSUGarnet are reasonably in good agreement with experimental flow data. The PNM EoS for the IOPB-I model is quite stiffer than G3 at high densities.

### C. Neutron stars

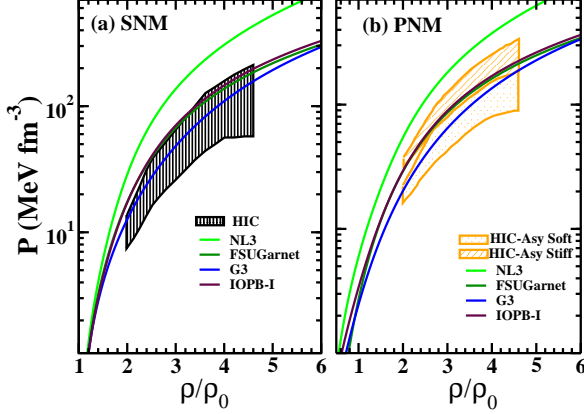


FIG. 5: (color online) Pressure as a function of baryon density for IOPB-I force. The results with NL3 [13], FSUGarnet [71], G3 [21] are compared with the EoS extracted from the analysis [105] for the (a) symmetric nuclear matter (SNM) and (b) pure neutron matter (PNM).

### (i) Predicted equation of states

We have solved Eqs.(22) and (23) for the energy density and pressure of the *beta-equilibrated* charge neutral neutron star matter. Fig. 6 displays the pressure as a function of energy density for the IOPB-I along with NL3, FSUGarnet and G3 sets. The solid circles are the central pressure and energy density corresponding to the maximum mass of the neutron star obtained from the above equations of state. The shaded region of the EoS can be divided into two parts as follows:

(i) Nättilä *et. al.* applied the Bayesian cooling tail method to constraint ( $1\sigma$  and  $2\sigma$  confidence limit) the EoS of cold densed matter inside the neutron stars [107].

(ii) Steiner *et. al.* have determined an empirical densed matter EoS with 95% confidence limit from a heterogeneous data set containing PRE bursts and quiescent thermal emission from X-ray transients [108].

From Fig. 6, it is clear that IOPB-I and FSUGarnet EoSs are similar at high-density but they differ remarkably at low densities as shown in the zoomed area of the inset. The NL3 set yields the stiffer EoS. Moreover, IOPB-I shows the stiffest EoS up to energy densities  $\mathcal{E} \lesssim 700 \text{ MeV fm}^{-3}$ . It can be seen that the results of IOPB-I at very high densities  $\mathcal{E} \sim 400 - 1600 \text{ MeV fm}^{-3}$  consistent with the EoS obtained by Nättilä and Steiner *et. al.* [107, 108]. But, FSUGarnet has a softer EoS at low energy densities  $\mathcal{E} \lesssim 200 \text{ MeV fm}^{-3}$  and stiffer EoS at intermediate energy densities as compared to that for the G3 set. One can conclude from Table III that the symmetry energy elements  $L$  and  $K_{sym}$  are smaller in G3 model compare to IOPB-I, FSUGarnet, and NL3. Hence, It yields the symmetry energy softer at higher density.

### (ii) Mass-radius and tidal deformability of neutron star

After fixing the equation of state for the various parameter sets, we extend our study to calculate the mass, radius and

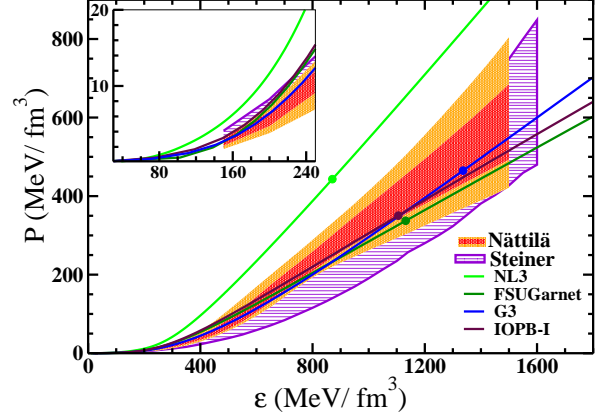


FIG. 6: (color online) The equations of states with NL3, FSUGarnet, G3 and IOPB-I for nuclear matter under charge neutrality as well as the  $\beta$ -equilibrium condition. The shaded region (violet) represents the observational constraint at  $r_{ph} = R$  with uncertainty of  $2\sigma$  [108]. Here,  $R$  and  $r_{ph}$  are the neutron star radius and the photospheric radius, respectively. Other shaded region (red+orange) represents the QMC+Model A equation of state of cold dense matter with 95% confidence limit [107]. The region zoomed near the origin is shown in the inset.

tidal deformability of a non-rotating neutron star. Placing a spherical star in a static external quadrupolar tidal field  $\mathcal{E}_{ij}$  results in deformation of the star along with quadrupole deformation which is the leading order perturbation. Such a deformation is measured by [30]

$$\lambda = -\frac{Q_{ij}}{\mathcal{E}_{ij}} = \frac{2}{3}k_2R^5; \quad (41)$$

$$\Lambda = \frac{2k_2}{3C^5}. \quad (42)$$

Where  $Q_{ij}$  is the induced quadrupole moment of a star in binary, and  $\mathcal{E}_{ij}$  is the static external quadrupole tidal field of the companion star.  $\lambda$  is the tidal deformability parameter depending on the EoS via both the neutron star (NS) radius and a dimensionless quantity  $k_2$ , called the second Love number [28, 30].  $\Lambda$  is the dimensionless version of  $\lambda$ , and  $C$  is the compactness parameter ( $C = M/R$ ). However, in general relativity (GR) we have to distinguish  $k_2$  between gravitational fields generated by masses (electric-type) and those generated by the motion of masses, *i.e.* mass currents (magnetic-type) [32, 109]. The electric tidal Love is found from the following expression [30]:

$$k_2 = \frac{8}{5}(1-2C)^2 C^5 [2C(y-1) - y + 2] \left\{ 2C(4(y+1)C^4 + (6y-4)C^3 + (26-22y)C^2 + 3(5y-8)C - 3y + 6) - 3(1-2C)^2(2C(y-1) - y + 2) \log\left(\frac{1}{1-2C}\right) \right\}^{-1}. \quad (43)$$

The value of  $y \equiv y(R)$  can be computed by solving the following first order differential equation [29, 32]:

$$r \frac{dy(r)}{dr} + y(r)^2 + y(r)F(r) + r^2 Q(r) = 0, \quad (44)$$

with,

$$F(r) = \frac{r - 4\pi r^3 [\mathcal{E}(r) - P(r)]}{r - 2M(r)}, \quad (45)$$

$$Q(r) = \frac{4\pi r(5\mathcal{E}(r) + 9P(r) + \frac{\mathcal{E}(r)+P(r)}{\partial P(r)/\partial \mathcal{E}(r)} - \frac{6}{4\pi r^2})}{r - 2M(r)} - 4 \left[ \frac{M(r) + 4\pi r^3 P(r)}{r^2(1 - 2M(r)/r)} \right]^2. \quad (46)$$

To estimate the tidal deformability  $\lambda$  of a single star, Eq.(44) must be integrated simultaneously with Tolman-Oppenheimer-Volkov (TOV) equations [110], *i.e.*

$$\frac{dP(r)}{dr} = - \frac{[\mathcal{E}(r) + P(r)][M(r) + 4\pi r^3 P(r)]}{r^2(1 - \frac{2M(r)}{r})}, \quad (47)$$

and

$$\frac{dM(r)}{dr} = 4\pi r^2 \mathcal{E}(r). \quad (48)$$

For a given EoS and from the boundary conditions  $P(0) = P_c$ ,  $M(0)=0$ , and  $y(0) = 2$ , where  $P_c$ ,  $M(0)$ , and  $y(0)$  are the central pressure, mass and dimensionless quantity. To obtain the tidal Love number, we solve this set of Eqs. (41-48) for a given EoS of the star at  $r=0$ . The value of  $r(=R)$ , where the pressure vanishes defines the surface of the star. Thus, at each central density we can uniquely determine a mass  $M$ , a radius  $R$  and tidal Love number  $k_2$  of the isolated neutron star using the chosen EoSs. In Fig. 7, the horizontal bars in cyan and magenta colours include the results from the precisely measured neutron stars masses, such as PSR J1614-2230 with mass  $M = 1.97 \pm 0.04 M_\odot$  [111] and PSR J0348+0432 with  $M = 2.01 \pm 0.04 M_\odot$  [112]. These observations imply that the maximum mass predicted by any theoretical model should reach the limit  $\sim 2.0 M_\odot$ . We also depict the  $1\sigma$  and  $2\sigma$  empirical mass-radius constraints for the cold densed matter inside the NS which have been obtained from a Bayesian analysis of type-I X-ray burst observation [107]. Similar approach is applied by Steiner *et. al.*, but they obtained the mass-radius from six sources, *i.e.*, three from transient low-mass X-ray binaries and three from type-I X-ray bursters with photospheric radius [108].

The NL3 model of RMF theory suggests a larger and massive NS with mass  $2.77 M_\odot$  and the corresponding NS radius to be 13.314 km, which is larger than the best observational radius estimates [107, 108]. Hence it is clear that the new RMF have been developed either through density-dependent couplings [52] or higher order couplings [21, 71]. These models successfully reproduce the ground-state properties of finite nuclei, nuclear matter saturation properties and also for the maximum mass of the neutron stars. Another important advantage of these models is that they are consistent with the sub-saturation density of the pure neutron matter. L. Rezzolla *et. al.* [113] have combined the recent gravitational-wave observation of merging system of binary neutron stars via the event GW170817 with quasi-universal relations between the maximum mass of rotating and non-rotating NSs. It is found that the maximum mass for non-rotating NS should be in the range  $2.01 \pm 0.04 \lesssim M(M_\odot) \lesssim 2.16 \pm 0.03$  [113], where the lower limit is observed from massive pulsars in the binary system [112]. From the results, we find that the maximum masses for IOPB-I along with FSUGarnet and G3 EoSs are consistent with the observed lower bound on the maximum NS mass. For the IOPB-I parametrization, the maximum mass of the NS is  $2.15 M_\odot$  and the radius (without including crust) of the *canonical* mass is 13.242 km which is relatively larger as compared to the current X-ray observations radii of range 10.5-12.8 km by Nättilä *et. al.* [107] and 11-12 km by Steiner *et. al.* [108]. Similarly, FSUGarnet fails to qualify radius constraint. However, recently E. Annala *et. al.* suggest that the radius of a  $1.4 M_\odot$  star should be in the range  $11.1 \leq R_{1.4 M_\odot} \leq 13.4$  km [114], which is consistent with the IOPB-I and FSUGarnet sets. Furthermore, G3 EoS is relatively softer at energy density  $\mathcal{E} \gtrsim 200 \text{ MeV fm}^{-3}$  (see in Fig. 6), which is able to reproduce the recent observational maximum mass of  $2.0 M_\odot$  as well as the radius of the *canonical* neutron star mass of 12.416 km.

Now we move to results for the tidal deformability of the single neutron star as well as binary neutron stars (BNS) which has been recently discussed in GW170817 [27]. The Eq. (41) indicates that  $\lambda$  strongly depends on the radius of the NS as well as on the value of  $k_2$ . Moreover,  $k_2$  depends on the internal structure of the constituent body and directly enters into the gravitational wave phase of inspiraling BNS which in turn conveys information about the EoS. As the radii of the NS increases, the deformation by the external field becomes large as there will be an increase in gravitational gradient with the simultaneous increase in radius. In other words, stiff (soft) EoS yields large (small) deformation in the BNS system. Fig. 8 shows the tidal deformability as a function of NS mass. In particular,  $\lambda$  takes a wide range of values  $\lambda \sim (1-8) \times 10^{36} \text{ g cm}^2 \text{ s}^2$  as shown in Fig. 8. For the G3 parameter set, the tidal

deformability  $\lambda$  is very low in the mass region  $0.5 - 2.0M_\odot$  in comparison with other sets. This is because the star exerts high central pressure and energy density resulting in the formation of a compact star which is shown as solid dots in Fig. 6. However, for the NL3 EoS case, it turns out that, because of the stiffness of the EoS, the  $\lambda$  value is increasing. The tidal deformability of the canonical NS ( $1.4M_\odot$ ) of IOPB-I along with FSUGarnet and G3 EoSs are found to be  $3.191 \times 10^{36}$ ,  $3.552 \times 10^{36}$ , and  $2.613 \times 10^{36} \text{ g cm}^2 \text{ s}^2$ , respectively as shown in Tables IV and V, which are consistent with the results obtained by Steiner *et al.* [115].

Next, we discuss the weighted dimensionless tidal deformability of the BNS of mass  $m_1$  and  $m_2$  and is defined as [27, 116, 117]:

$$\tilde{\Lambda} = \frac{8}{13} \left[ (1 + 7\eta - 31\eta^2)(\Lambda_1 + \Lambda_2) + \sqrt{1 - 4\eta}(1 + 9\eta - 11\eta^2)(\Lambda_1 - \Lambda_2) \right], \quad (49)$$

with tidal correction

$$\delta\tilde{\Lambda} = \frac{1}{2} \left[ \sqrt{1 - 4\eta} \left( 1 - \frac{13272}{1319}\eta + \frac{8944}{1319}\eta^2 \right) (\Lambda_1 + \Lambda_2) + \left( 1 - \frac{15910}{1319}\eta + \frac{32850}{1319}\eta^2 + \frac{3380}{1319}\eta^3 \right) (\Lambda_1 - \Lambda_2) \right]. \quad (50)$$

Here,  $\eta = m_1 m_2 / M^2$  is the symmetric mass ratio,  $m_1$  and  $m_2$  are the binary masses,  $M = m_1 + m_2$  is the total mass,  $\Lambda_1$  and  $\Lambda_2$  are the dimensionless tidal deformability of BNS, for the case  $m_1 \geq m_2$ . Also, we have taken equal and unequal-masses ( $m_1$  and  $m_2$ ) BNS system as it has been done in Refs. [118, 119]. The calculated results for the  $\Lambda_1$ ,  $\Lambda_2$  and weighted tidal deformability  $\tilde{\Lambda}$  of the present EoSs are displayed in Tables IV and V. In Fig. 9, we display the different dimensionless tidal deformabilities corresponding to progenitor masses of the NS. It can be seen that the IOPB-I along with FSUGarnet and G3 are in good agreement with the 90% and 50% probability contour of GW170817 [27]. Recently, aLIGO/VIRGO detectors have measured the value of  $\tilde{\Lambda}$  whose results are more precise than the results found by considering the individual value of  $\Lambda_1$  and  $\Lambda_2$  of the BNS [27]. It is noticed that the value of  $\tilde{\Lambda} \leq 800$  in the low-spin case and  $\tilde{\Lambda} \leq 700$  in the high spin case within the 90% credible intervals which are consistent with the 680.79, 622.06 and 461.03 of the  $1.4M_\odot$  NS binary for the IOPB-I, FSUGarnet and G3 parameter sets, respectively (see Tables IV and V). We also find a reasonably good agreement in the  $\tilde{\Lambda}$  value equal to 582.26 for  $1.35M_\odot$  in the G3 EoS, which is obtained using a Markov Chain Monte Carlo simulation of BNS with  $\tilde{\Lambda} \approx 600$  at signal-to-noise ratio of 30 in a single aLIGO detector [116, 117]. Finally, we close this section with the discussion on chirp mass  $\mathcal{M}_c$  and chirp radius  $\mathcal{R}_c$  of the BNS system which are defined as:

$$\mathcal{M}_c = (m_1 m_2)^{3/5} (m_1 + m_2)^{-1/5} \quad (51)$$

$$\mathcal{R}_c = 2\mathcal{M}_c \tilde{\Lambda}^{1/5}. \quad (52)$$

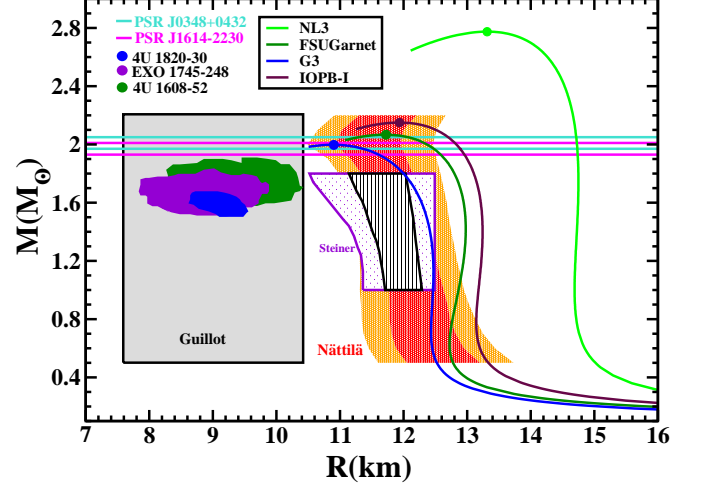


FIG. 7: (color online) The mass-radius profile predicted by NL3, FSUGarnet, G3 and IOPB-I. The recent observational constraints on neutron-star masses [111, 112] and radii [107, 108, 120, 121] are also shown.

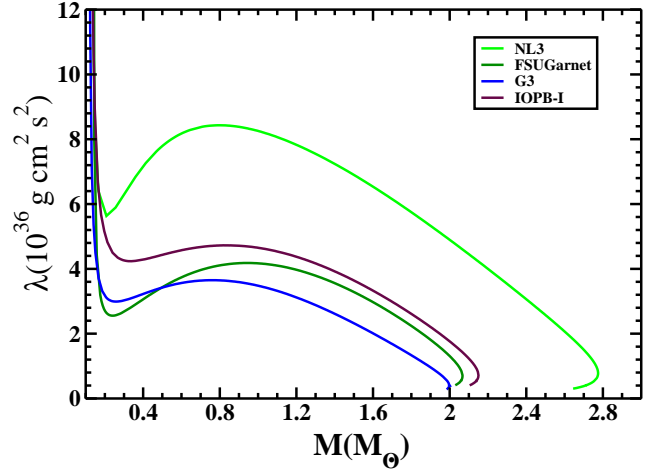


FIG. 8: (color online) The tidal deformability  $\lambda$  as a function of neutron star mass with different EoSs.

The precise mass measurements of the NSs have been reported in Refs. [111, 112]. However, till now no observation has been confirmed regarding the radius of the most massive NS. Recently, aLIGO/VIRGO has measured chirp mass  $1.188^{+0.004}_{-0.002} M_\odot$  with very good precision. With the help of this, we can easily calculate the chirp radius  $\mathcal{R}_c$  of the BNS system and we find that the chirp radius is in the range between  $7.867 \leq \mathcal{R}_c \leq 10.350 \text{ km}$  for equal and unequal-mass BNS system as shown in Tables IV and V.

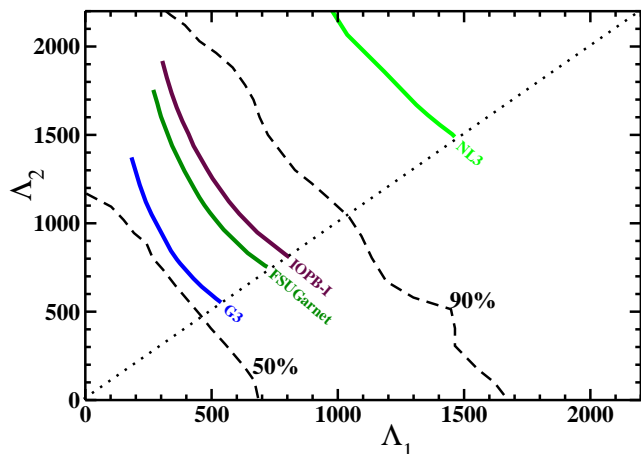


FIG. 9: (color online) Different values of  $\Lambda$  generated by using IOPB-I along with NL3, FSUGarnet and G3 EoSs are compared with the 90% and 50% probability contour in case of low-spin  $|\chi| \leq 0.05$  as given in Fig. 5 of GW170817 [27].

## V. SUMMARY AND CONCLUSIONS

We have built a new relativistic effective interaction for finite nuclei, infinite nuclear matter and neutron stars. The optimization has been done using experimental data for eight

spherical nuclei such as binding energy and charge radius. The prediction of observables such as binding energies and radii with the new IOPB-I set for finite nuclei are quite good. The  $Z=120$  isotopic chain shows that the magicity appears at neutron numbers  $N=172, 184,$  and  $198$ . Furthermore, we find that the IOPB-I set yields slightly larger values for the neutron-skin thickness. This is due to the small strength of the  $\omega - \rho$  cross-coupling. For infinite nuclear matter at sub-saturation and supra-saturation densities, the results of our calculations agree well with the known experimental data. The nuclear matter properties obtained by this new parameter set are: nuclear incompressibility  $K = 222.65$  MeV, symmetry energy coefficient  $J = 33.30$  MeV, symmetry energy slope  $L = 63.6$  MeV, and the asymmetry term of nuclear incompressibility  $K_\tau = 389.46$  MeV at saturation density  $\rho_0 = 0.149$  fm $^{-3}$ . In general, all these values are consistent with current empirical data. The IOPB-I model satisfies the density dependence of symmetry energy which is obtained from the different sets of experimental data. It also yields the NS maximum mass to be  $2.15M_\odot$  which is consistent with the current GW170817 observational constraint [113]. The radius of the canonical neutron star is 13.24 km compatible with the theoretical results in Ref. [114]. Similarly, the predicted values of dimensionless tidal deformabilities are in accordance with the GW170817 observational probability contour [27].

**Acknowledgments:** Bharat Kumar would like to take this opportunity to convey special thanks to P. Landry and Joonas Nättilä, fruitful discussions, and useful suggestions. Further, Bharat Kumar thankful to Swagatika Bhoi for careful reading of the manuscript.

- 
- [1] R. J. Furnstahl, B. D. Serot and H. B. Tang, Nucl. Phys. A **598**, 539 (1996); R. J. Furnstahl, B. D. Serot and H. B. Tang, Nucl. Phys. A **615**, 441 (1997).
- [2] P. Arumugam, B. K. Sharma, P. K. Sahu, S. K. Patra, Tapas Sil, M. Centelles, and X. Viñas, Phys. Lett. B **601**, 51 (2004).
- [3] M. Del Estal, M. Centelles, X. Viñas and S. K. Patra, Phys. Rev. C **63**, 024314 (2001).
- [4] E. Chabanat, P. Bonche, P. Haensel, J. Meyer, and R. Schaeffer, Nucl. Phys. A **635**, 231 (1998).
- [5] N. Sandulescu, Nguyen Van Giai, and R. J. Liotta, Phys. Rev. C **61**, 061301(R) (2000).
- [6] J. Dobaczewski, H. Flocard, and J. Treiner, Nucl. Phys. A **422**, 103 (1984).
- [7] J. Dobaczewski, W. Nazarewicz, T. R. Werner, J. F. Berger, R. C. Chin, and J. Decharge, Phys. Rev. C **53**, 2809 (1996).
- [8] J. Dechargé and D. Gogny, Phys. Rev. C **21**, 1568 (1980).
- [9] J. D. Walecka, Ann. Phys. (N. Y.) **83**, 491 (1974).
- [10] J. Boguta and A. R. Bodmer, Nucl. Phys. A **292**, 413 (1977).
- [11] P. -G. Reinhard, Rep. Prog. Phys. **52**, 439 (1989).
- [12] M. M. Sharma, G. A. Lalazissis and P. Ring, Phys. Lett. B **317**, 9 (1993).
- [13] G. A. Lalazissis, J. König and P. Ring, Phys. Rev. C **55**, 540 (1997).
- [14] G. A. Lalazissis, S. Karatzikos, R. Fossion, D. Pena Arteaga, A. V. Afanasjev and P. Ring, Phys. Lett. B **671**, 36 (2009).
- [15] A. R. Bodmer, Nucl. Phys. A **526**, 703 (1991)
- [16] S. Gmuca, Nucl. Phys. A **547**, 447 (1992); J. K. Bunta and S. Gmuca, Phys. Rev. C **68**, 054318 (2003).
- [17] Y. Sugahara and H. Toki, Nucl. Phys. A **579**, 557 (1994).
- [18] D. Vretenar, G. A. Lalazissis and P. Ring, Phys. Rev. C **62**, 045502 (2000).
- [19] B. G. Todd-Rutel and J. Piekarewicz, Phys. Rev. Lett. **95**, 122501 (2005); C. J. Horowitz and J. Piekarewicz, Phys. Rev. Lett. **86**, 5647 (2001); Phys. Rev. C **64**, 062802 (R) (2001).
- [20] S. Kubis and M. Kutschera, Phys. Lett. B **399**, 191 (1997).
- [21] Bharat Kumar, S. K. Singh, B. K. Agrawal, S. K. Patra Nucl. Phys. A **966**, 197 (2017).
- [22] G. Ferini, M. Colonna, T. Gaitanos and M. Di Toro, Nucl. Phys. A **762**, 147 (2005).
- [23] H. Chiu and E. E. Salpeter, Phys. Rev. Lett. **12**, 413 (1964).
- [24] J. N. Bahcall and R. A. Wolf, Phys. Rev. Lett. **14**, 343 (1965).
- [25] J. M. Lattimer, C. J. Pethic, M. Prakash and P. Haensel, Phys. Rev. Lett. **66**, 2701 (1991).
- [26] C. J. Horowitz, S. J. Pollock, P. A. Souder and R. Michaels, Phys. Rev. C **63**, 025501 (2001).
- [27] P. B. Abbott *et al.*, Phys. Rev. Lett. **119**, 161101 (2017).
- [28] É.É. Flanagan and T. Hinderer, Phys. Rev. D **77**, 021502 (2008).
- [29] T. Hinderer, Astrophys. J. **677**, 1216 (2008); 697964(E) (2009).
- [30] T. Hinderer, B. D. Lackey, R. N. Lang, and J. S. Read, Phys. Rev. D **81**, 123016 (2010).
- [31] J. M. Lattimer and M. Prakash, Phys. Rept. **442**, 109 (2007).
- [32] Bharat Kumar, S. K. Biswal and S. K. Patra, Phys. Rev. C **95**,

- 015801 (2017).
- [33] B. K. Agrawal, S. Shlomo and V. K. Au, Phys. Rev. C **72**, 014310 (2005).
- [34] B. K. Agrawal, Shashi K. Dhiman and Raj Kumar, Phys. Rev. C **73**, 034319 (2006).
- [35] Raj Kumar, B. K. Agrawal and Shashi K. Dhiman, Phys. Rev. C **74**, 034323 (2006).
- [36] H. Müller and B. D. Serot, Nucl. Phys. A **606**, 508 (1996).
- [37] B. D. Serot and J. D. Walecka, Int. J. Mod. Phys. E **6**, 515 (1997).
- [38] S. K. Singh, S. K. Biswal, M. Bhuyan, S. K. Patra, Phys. Rev. C **89**, 044001 (2014).
- [39] R. J. Furnstahl, C. E. Price and G. E. Walker, Phys. Rev. C **36**, 2590 (1987).
- [40] J. P. Elliott and T. H. R. Skyrme, Proc. Soc. (London) A **232**, 561 (1955).
- [41] J. W. Negele Phys. Rev. C **1**, 1260 (1970).
- [42] J. M. Eisenberg and W. Greiner, *Microscopic Theory of the Nucleus* (North-Holland, Amsterdam, 1972).
- [43] P. Ring and P. Schuck, *The Nuclear Many-Body Problem* (Springer-Verlag, Berlin, 1980).
- [44] Y. K. Gambhir, P. Ring and A. Thimet, Ann. Phys. (N.Y.) **198**, 132 (1990).
- [45] P. -G. Reinhard, M. Rufa, J. Maruhn, W. Greiner and J. Friedrich, Z. Phys. A **323**, 13 (1986).
- [46] Y. Sugahara and H. Toki, Nucl. Phys. A **579**, 557 (1994).
- [47] E. Chabanat, P. Bonche, P. Haensel, J. Meyer and R. Schaeffer, Nucl. Phys. A **635**, 231 (1998).
- [48] N. Sandulescu, Nguyen Van Giai and R. J. Liotta, Phys. Rev. C **61**, 061301(R) (2000).
- [49] B. D. Serot and J. D. Walecka, Adv. Nucl. Phys. **16**, 1 (1986).
- [50] W. Kohn and L. J. Sham, Phys. Rev. A **140**, 1133 (1965); C. Speicher, R. M. Dreizler, and E. Engel, Ann. Phys. N.Y. **213**, 312 (1992).
- [51] T. Matsui, Nucl. Phys. A **370**, 365 (1981).
- [52] X. Roca-Maza, X. Viñas, M. Centelles, P. Ring and P. Schuck, Phys. Rev. C **84**, 054309 (2011).
- [53] S. K. Singh, M. Bhuyan, P. K. Panda and S. K. Patra, J. Phys. G: Nucl. Part. Phys. **40**, 085104 (2013).
- [54] C. J. Horowitz and J. Piekarewicz, Phys. Rev. C **64**, 062802 (R) (2001).
- [55] L. -W. Lattimer, B. -J. Cai, C. M. Ko, B. -A. Li, C. Shen and J. Xu, Phys. Rev. C **80**, 014322 (2009).
- [56] M. B. Tsang et al., Phys. Rev. C **86**, 15803 (2012).
- [57] M. Dutra et al., Phys. Rev. C **85**, 035201 (2012).
- [58] C. Xu, B.-A. Li and L.-W. Chen, Phys. Rev. C **82**, 054607 (2010).
- [59] W. G. Newton, M. Gearheart and B.-A. Li, arXiv:1110.4043.
- [60] A. W. Steiner and S. Gandolfi, Phys. Rev. Lett. **108**, 081102 (2012).
- [61] F. J. Fattoyev, W. G. Newton, J. Xu and B.-A. Li, Phys. Rev. C **86**, 025804 (2012).
- [62] M. Centelles, X. Roca-Maza, X. Viñas and M. Warda, Phys. Rev. Lett. **102**, 122502 (2009).
- [63] B. A. Li and X. Han, Phys. Lett. B **727**, 276 (2013).
- [64] S. Kirkpatrick, C. D. Gelatt and M. P. Vecchi, Science **220**, 671 (1983).
- [65] W. H. Press, S. A. Teukolsky, W. T. Vetterling and B. P. Flannery, Numerical Recipes in Fortran, (*Cambridge University Press, New York*, 1992).
- [66] S. Kirkpatrick, J. Stat. Phys. **34**, 975 (1984).
- [67] L. Ingber, Math. Comput. Model. **12**, 967 (1989).
- [68] B. Cohen, Masters thesis, Tel-Aviv University, 1994.
- [69] J. Dobaczewski, W. Nazarewicz and P. -G. Reinhard, J. Phys. G: Nucl. Part. Phys. **41**, 074001 (2014).
- [70] P. Klüpfel, P. -G. Reinhard, T. J. Bürvenich, and J. A. Maruhn, Phys. Rev. C **79**, 034310 (2009).
- [71] Wei-Chai Chen and J. Piekarewicz, Phys. Lett. B **748**, 284 (2015).
- [72] M. Wang, G. Audi, A. H. Wapstra, F. G. Kondev, M. MacCormick, X. Xu and B. Pfeiffer, Chin. Phys. C **36**, 1603 (2012).
- [73] I. Angeli, K. P. Marinova, At. Data and Nucl. Data Tables **99**, 69 (2013).
- [74] A. Trzcińska, J. Jastrzebski, P. Lubiński, F. J. Hartmann, R. Schmidt, T. von Egidy, and B. Klos, Phys. Rev. Lett. **87**, 082501 (2001); J. Jastrzębski, A. Trzcińska, P. Lubiński, B. Klos, F. J. Hartmann, T. von Egidy, S. Wycech, Int. J. Mod. Phys. E **13** (2004) 343.
- [75] S. K. Patra, Int. J. Mod. Phys. E **2**, 471 (1993).
- [76] R. F. Garcia Ruiz et. al., Nature Phys. **12**, 594 (2016).
- [77] P. -G. Reinhard and W. Nazarewicz, Phys. Rev. C **81**, 051303 (R) (2010).
- [78] X. Roca-Maza, M. Centelles, X. Viñas, and M. Warda, Phys. Rev. Lett. **106**, 252501 (2011).
- [79] B. A. Brown, Phys. Rev. Lett. **85**, 5296 (2000).
- [80] S. Abrahamyan et. al., Phys. Rev. Lett. **108**, 112502 (2012).
- [81] X. Viñas, M. Centelles, X. Roca-Maza and M. Warda, Eur. Phys. J. A **50** (2014) 27.
- [82] F. J. Fattoyev, J. Piekarewicz and C. J. Horowitz, arXiv:1711.06615v1.
- [83] P. Möller, A. J. Sierk, T. Ichikawa, and H. Sagawa, At. Data Nucl. Data Tables **109**, 1 (2016).
- [84] J. Zenihiro et. al., Phys. Rev. C **82**, 044611 (2010).
- [85] K. Rutz, M. Bender, T. Bürvenich, T. Schilling, P. -G. Reinhard, J. A. Maruhn and W. Greiner, Phys. Rev. C **56**, 238 (1997).
- [86] R. K. Gupta, S. K. Patra and W. Greiner, Mod. Phys. Lett. A **12**, 1727 (1997).
- [87] S. K. Patra, C. -L. Wu, C. R. Praharaaj and R. K. Gupta, Nucl. Phys. A **651**, 117 (1999).
- [88] M. S. Mehta, Harvinder Kaur, Bharat Kumar, and S. K. Patra, Phys. Rev. C **92**, 054305 (2015).
- [89] M. Bhuyan and S. K. Patra, Mod. Phys. Lett. A **27**, 1250173 (2012).
- [90] P. Danielewicz and J. Lee, Nucl. Phys. A **922**, 1 (2014).
- [91] M. B. Tsang, Y. Zhang, P. Danielewicz, M. Famiano, Z. Li, W. G. Lynch, and A. W. Steiner, Phys. Rev. Lett. **102**, 122701 (2009); Int. J. Mod. Phys. E **19**, 1631 (2010).
- [92] P. Russotto et al., Phys. Rev. C **94**, 034608 (2016).
- [93] G. Coló, U. Garg, and H. Sagawa, Eur. Phys. J. A **50**, 26 (2014).
- [94] J. Piekarewicz, Eur. Phys. J. A **50**, 25 (2014).
- [95] J. R. Stone, N. J. Stone, and S. A. Moszkowski, Phys. Rev. C **89**, 044316 (2014).
- [96] J. M. Pearson, N. Chamel, and S. Goriely, Phys. Rev. C **82**, 037301 (2010).
- [97] T. Li et. al., Phys. Rev. C **81**, 034309 (2010).
- [98] U. Garg et. al., Nucl. Phys. A **788**, 36 (2007).
- [99] M. Baldo and C. Maieron, Phys. Rev. C **77**, 015801 (2008).
- [100] B. Friedman and V. R. Pandharipande, Nucl. Phys. A **361**, 502 (1981).
- [101] S. Gandolfi, A. Yu. Illarionov, S. Fantoni, F. Pederiva, and K. E. Schmidt, Phys. Rev. Lett. **101**, 132501 (2008).
- [102] A. Gezerlis and J. Carlson, Phys. Rev. C **81**, 025803 (2010).
- [103] K. Hebeler, J. M. Lattimer, C. J. Pethick and A. Schwenk, Astrophys. J. **773**, 11 (2013).
- [104] C. Mondal, B. K. Agrawal, J. N. De, and S. K. Samaddar Phys.

- Rev. C **93**, 044328 (2016).
- [105] P. Danielewicz, R. Lacey, and W. G. Lynch, *Science* **298**, 1592 (2002).
- [106] M. Praksh, T. L. Ainsworth and J. M. Lattimer, *Phys. Rev. Lett.* **61**, 2518 (1988).
- [107] J. Nättilä, A. W. Steiner, J. J. E. Kajava, V. F. Suleimanov and J. Poutanen, *A. & A.* **591**, 25 (2016).
- [108] A. W. Steiner, J. M. Lattimer and E. F. Brown, *Astrophys. J.* **722**, 33 (2010).
- [109] P. Landry and Eric Poisson, *Phys. Rev. D* **89**, 124011 (2014).
- [110] J. R. Oppenheimer and G. M. Volkoff, *Phys. Rev.* **55**, 374 (1939); R. C. Tolman, *ibid.* **55**, 364 (1939).
- [111] P. B. Demorest, T. Pennucci, S. M. Ransom, M. S. E. Roberts, and J. W. T. Hessels, *Nature (London)* **467**, 1081 (2010).
- [112] J. Antoniadis et al., *Science* **340**, 6131 (2013).
- [113] L. Rezzolla, Elias R. Most and Lukas R. Weth, arXiv:1711.00314v1.
- [114] Eemeli Annala, Tyler Gorda, Alekski Kurkela and Alekski Vuorinen, arXiv:1711.02644v1.
- [115] A. W. Steiner, S. Gandolfi, F. J. Fattoyev, and W. G. Newton, *Phys. Rev. C* **91**, 015804 (2015).
- [116] M. Favata, *Phys. Rev. Lett.* **112**, 101101 (2014).
- [117] L. Wade, J. D. E. Creighton, E. Ochsner, B. D. Lackey, B. F. Farr, T. B. Littenberg, and V. Raymond, *Phys. Rev. D* **89**, 103012 (2014).
- [118] P. B. Abbott *et. al.*, arXiv:1710.09320v1.
- [119] D. Radice, A. Perego and F. Zappa, arXiv:1711.03647v1.
- [120] F. Ozel, G. Baym and T. Guver, *Phys. Rev. D* **82**, 101301 (2010).
- [121] V. Suleimanov, J. Poutanen, M. Revnivtsev and K. Werner, *Astrophys. J.* **742**, 122 (2011).